UNIVERSITY COLLEGE LONDON

Interatomic Potentials and $BaTiO_3$: A study on which interatomic potentials provide an accurate reproduction of the structural phase behaviour of $BaTiO_3$

CHEMGM01 Research Project
17130693

Submitted for the award of
MRes Molecular Modelling and Materials Science

in the

Centre for Doctoral Training in Molecular Modelling and Materials Science,
Department of Chemistry,
UCL

September, 2018

Abstract

Multiple structural optimisations are performed for the phase transitions of Barium Titanate, employing four different potential input libraries. The results were then studied to see how each set of interatomic potentials performed, and whether they accurately reproduced the structure of each phase. It was found that the interatomic potentials derived by Freeman et. al. (Freeman, C. L.; Dawson, J. A.; Chen, H.-R.; Harding, J. H.; Ben, L.-B.; Sinclair, D. C.J. Mater. Chem.2011,21, 4861–4868), provide results close to experimental values, though not without careful considerations for the optimisation process.

Acknowledgements

I would like to thank my supervisor, for providing me with insight and opportunities throughout the course of this project, the course coordinators who gave valuable help towards completion of the project, and my course mates who went through the same journey. I'd also like to thank my family, and my friends both new and old who added to my overall well-being during this project.

Contents

1 Introduction

Barium Titanate, $BaTiO_3$ (BTO), is a ferroelectric oxide[1] and due to these properties, it has seen substantial use in electrical industries due to its very high dielectric constant[2, 3]. BTO was the first polycrystalline ceramic material to be found that showcased ferroelectricity and the material was initially used for piezoelectric ceramic transducers applications[4]. BTO has been employed extensively in a variety of modern technologies such as actuators, sensors, thin-film memories, energy harvesting, transducers, multilayer ceramic capacitors and nanocarriers for drug delivery[5–8].

However, despite seeing plenty of attention as a transducer during the 40's and 50s, it was replaced due to the discovery of lead zirconate-titanate (PZT)[9]. PZT is a material with better piezoelectric properties and higher Curie temperature Tc than BTO, which led to a significant reduction in interest of BTO for piezoelectric applications[10]. Incidentally, as knowledge of lead's toxicity gained more knowledge, and its impact on the environment was studied subsequently resulting in calls by the European Union for more environmentally friendly materials, as well regulation of lead and other toxic materials[11, 12]. Interest in ferroelectric alternatives grew as research was encouraged to develop lead-free piezoelectrics.

Saito et al.[13] reported in 2004 of an alkaline-niobate-based lead-free piezoelectrics with comparable properties to PZT, resulting in great interest to research lead-free piezoelectrics. In the wake of this publication, the scientific community revisited the work done by Takenaka et al.[14] in 1991, where BTO was utilized by the group and the effect of a morphotropic phase boundary (MPB) lead to changes in the dielectric and piezoelectric properties. Later on, Lui and Ren[15] in 2009, reconsidered the use of BTO-based materials for piezoelectric materials, modifying BTO with Ca and Zr to achieve a significant improvement in electromechanical properties. This discovery allowed BTO-based materials to be model system for furthering understanding of the underlying physics of lead-free piezoelectric materials and advancement of their design[16]. As a result this has led to BTO-based materials to have seen increased research in recent years as shown in figure 1.

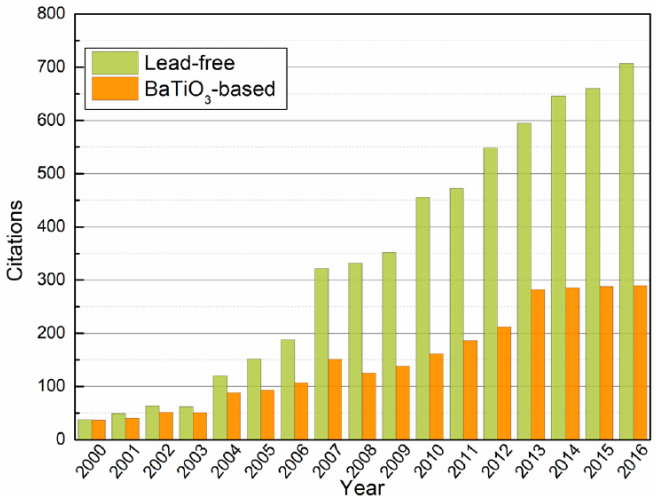

FIGURE 1 The number of research papers released related to the study of lead-free and BTO-based piezoelectrics[16].

Further research has been conducted on improving or altering the piezoelectric and dielectric properties of BTO. One example includes engineering the domains of BTO, with things such as domain wall motion, defect doping, engineering the twin boundaries that occur, and crystal structure control (such as epitaxial strain). Research in this area has improved understanding of the ferroelectric, increasing its potential as lead-free piezoelectric substitute[16,

17].

As computer processing power has increased with modern technological advancements, the cost of running computer simulations on crystal structures has gone down, which has resulted in quicker results, as well as allowing more complex simulations to be done. Utilizing tools available, it was decided that such simulations were to be performed on BTO to create an accurate representation such that further modifications could be performed to verify recent scientific literature or to enhance experimental work.

Through further study of the material computationally, it is hoped that a good understanding of the material can be gathered, and then progressed either experimentally or computationally. Computational development would focus on refining the material to achieve certain desired characteristics, predicting new structures through doping or other manipulations, or confirming manufactured ones. Experimental development would entail the use of coherent Bragg X-rays to probe already manufactured BTO nanocrystals. Particularly, it would be focused on the twin boundaries of BTO, which present themselves under certain growth circumstances, and it would explored whether it is an area of interest. In either case, starting simply is the first step towards a deeper understanding of how to improve the BTO structure that would result in it being a lead-free alternative.

Through the use of The General Utility Lattice Program, GULP[18], the groundwork is laid upon which further analysis of BTO crystal structures can be performed. GULP has a strong emphasis on lattice dynamical methods, such that it utilizes a statistical mechanical treatment which results in the output of thermodynamic properties such as free-energy and can be used to analyse phonon vibrational modes. Future treatment would involve utilizing the costlier molecular dynamics methods or Monte Carlo simulations to assess the effect of temperature on BTO and comparing it to initial lattice dynamic results.

This project focuses on the effect that various potential models have on the BTO lattice at different phases, in the hopes that the characteristics of the structural phase transitions of BTO can be accurately reproduced. The efficacy of each potential model is discussed, further which model, or combination of models, is to be used for future analysis. Due to the nature of BTO's ferroelectric behaviour which comes as a result of soft modes, the parameters of energy minimisation are studied to see whether the final result is a more accurate description of this behaviour.

After such calculations are performed, it was hoped that these results would then be transferred onto different structures of BTO, such as those with grain boundaries or twin structures contained in the structure to further develop understanding of its behaviour. Optimistically, these results could then be transferred to reproducing structures in the literature, to accompany experiments on the material looking at the Curie temperature. Despite coming short of being able to perform such calculations in this project, the background is still discussed as it was the primary motivation for studying this material.

2 Background

2.1 Phase Transitions

Belonging to the ABO_3 family of $CaTiO_3$, BTO has a tetragonally skewed perovskite crystal structure at ambient temperature[19]. To be classed as a crystal that exhibits this behaviour, the A and B metal ions must each possess different radii, with the radially larger atom having the smaller charge of the 2. This overall charge from the A and B ions is +6[19]. When there is a fluctuation in temperature, BTO undergoes several structural phase transitions as a result of crossing temperature thresholds of those phases[10, 20].

At ambient pressures, when BTO is at a very high temperature, it is in the hexagonal space group $P6_3/mm$, changing its structure at 1733K to enter the centrosymmetric cubic perovskite structural phase ($Pm\bar{3}m$), where it remains for a while. In this schematic, the Ba^{2+} ions are located on the A-site, which is positioned at the corners of the cubic unit cell, whereas Ti^{4+} ions occupy the B-sites located in the cell center, and oxygen anions are located at the face centers of the unit cell and constitute BO_6 octahedra[10, 21].

As it approaches lower temperatures, it reaches the ferroelectric Curie temperature at 393K[22]. At the Curie temperature, the amplitude of a transverse optic mode condenses, which is related to the spontaneous polarisation and determines the order for the transition of the cubic phase into lower symmetry phases[10]. As the temperature decreases below the Curie temperature, it is seen that BTO goes through a sequence of successive first-order phase transitions. Cooling BTO below the Curie temperature, BTO undergoes a phase transition to form a tetragonal phase (*P4mm*). Further phase transitions occur as temperatures cool further, changing to orthorhombic (*Amm2*) at 278K and to the rhombohedral structural phase (*R3m*) at 183K[2, 3, 10, 21, 23]. This is shown in figure 2.

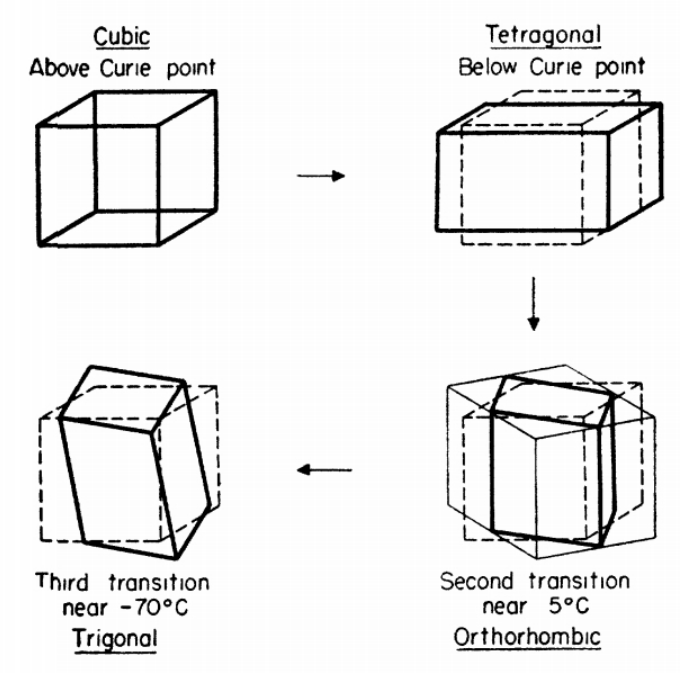

FIGURE 2 The paraelectric to ferroelectric phase transitions of BTO in a clockwise fashion[23].

2.2 Ferroelectricity

The piezoelectric effect is described as the linear coupling interaction between the mechanical and electrical fields in a crystalline material. It is the resultant electric charge that accumulates on the surface of a piezoelectric material when it is subjected to applied mechanical stress. This is known as the direct piezoelectric effect. It is a reversible process, in that it exhibits both the generation of electrical energy as a result from mechanical stress, and furthermore, if an external electrical field is applied to the material, this results in the generation of a mechanical strain, known as the reverse piezoelectric effect. This mechanical strain causes the material dimensions to be changed, which is dependent on the direction of the applied electric field, which leads to either expansion or contraction of the material.

Of the 32 crystal classes, piezoelectricity is directly exhibited by 20 crystal classes. Within these 20 classes, 10 exhibit what is known as pyroelectricity, or polar dielectrics, whereby there exists polar axis with a direction which is dictated by symmetry. Temperature or pressure does not bare any effect on the orientation of the polar axis, but the magnitude of the polarisation is altered by varying the temperature, known as the pyroelectric effect.

Within these pyroelectric classes, materials which exhibit a reversible natural electrical polarisation, are known as ferroelectrics. In the absence of an electric field, ferroelectrics are polar materials that showcases at least two equilibrium orientations of spontaneous polarisation. Reorientation of the polarisation can be carried out through an

applied electric field. The polarisation in ferroelectrics is not just a function of the applied electric field – found in paraelectric materials – but also dependant on its history, which yields hysteresis curves.

Below the Curie temperature, the tetragonal, orthorhombic, and rhombohedral phases exhibit ferroelectricity, and for the cubic phase above the Curie temperature, it exhibits paraelectricity. At the phase transitions of the BTO, it showcases a strong dielectric softening at each transition, and changes in the dielectric constant has three maxima peaks in relative permittivity, shown in figure 3.

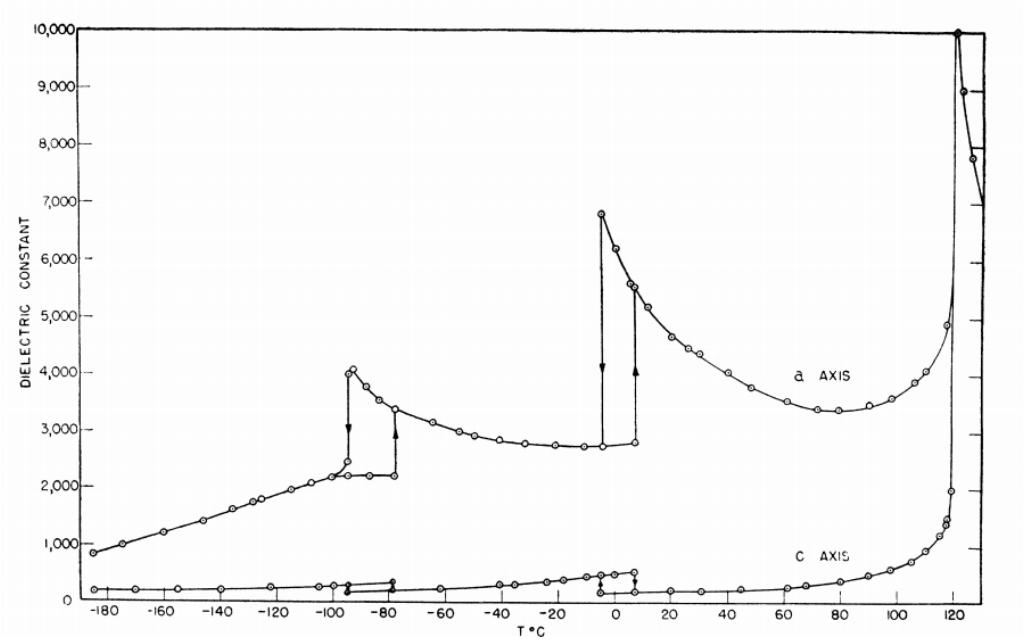

FIGURE 3 Initial dielectric constants parallel to the *a*- and *c*-axes[23].

Devonshire[24, 25] developed a phenomenological theory of BTO which provided the initial unified description of the observed changes in crystal structure, and variations of thermal, mechanical, dielectric, and piezoelectric properties as BTO experiences the different phase transitions. It was assumed that nonlinear behaviour of the dielectric response is responsible for the observed differences in the material.

The permanent dipole moments in ferroelectricity are a consequence of cation and anion displacements from equilibrium, in the opposite directions, which leads to the generation of ferroelectricity in BTO. These transitions are characterized by whether the transition is displacement type or order-disorder type, although some transitions are a product of both types[26].

Displacement type transitions has a mechanism whereby at the ferroelectric phase transition point, the cations and anions return to their equilibrium positions. At which point the dipoles disappear. BTO has long considered to be of the displacive type, with low temperature phases involving rotations of macroscopic polarisation. In the rhombohedral phase, this polarisation is parallel to the (111) crystal axis. Heating the crystal results in the polarisation aligning parallel to the orthorhombic (011) axis, and eventually with the tetragonal (001) axis, after which the cations and anions return to equilibrium and the polarisation disappears[27].

In the displacement model, softening of relevant phonon modes as the transition temperatures is approached on the descent results in the displacements of atoms. As the frequency becomes negative, the mode becomes unstable, and that results in the displacement found in the lower symmetry phase[28]. For most properties of BTO, this successfully describes much of thermodynamics of the system, as well as providing explanation for the cause of the structural and ferroelectric phase transitions.

However, this model does not the vanishing of first-order Raman excitation in the cubic phase due to microscopic inversion symmetry[29], contradicts X-ray fine structure experiments[27] which shows the displacement directions of the Ti atoms, and doesn't cover heavily-damped non-zero soft phonon modes[30].

The order-disorder model describes certain systems whereby a spontaneous symmetry breaking occurs, in which all the Ti atoms are located in one of the potential 8 minima along the <111> directions for all crystal systems[31–33]. A diagram of this is shown in figure 4.

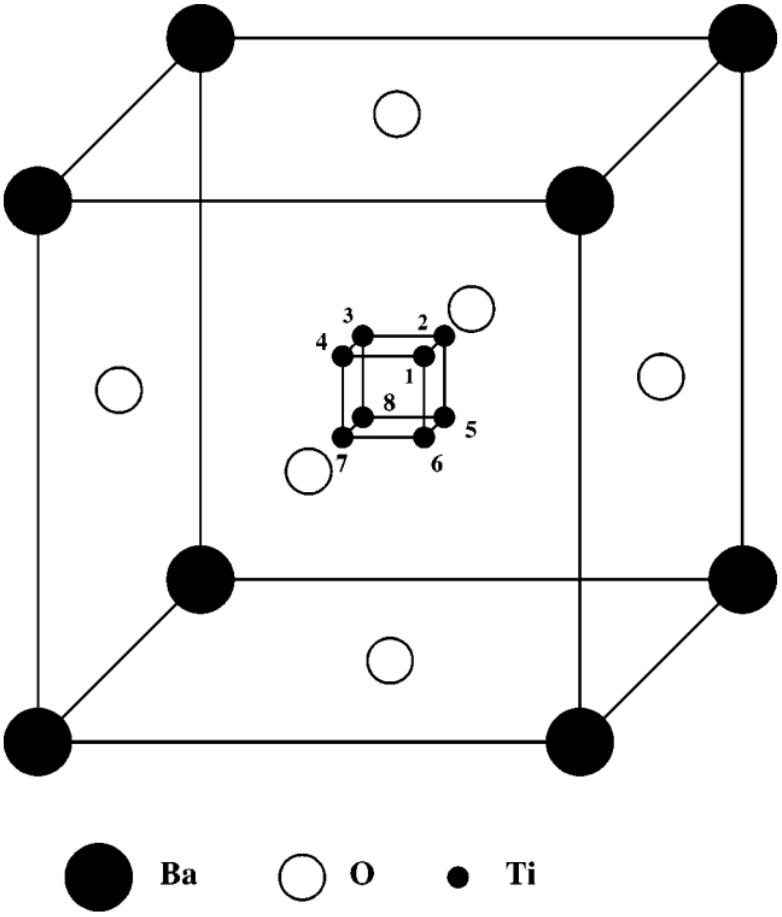

FIGURE 4 A schematic diagram which depicts the cubic unit cell of BTO, depicting the eight possible off-center displacements that the Ti can undergo in the [111] direction[34].

This model also has some shortcomings, as it fails to predict the observed heavily damped low frequency soft modes near the phase transition, as evidenced by neutron scattering experiments[31]. It also results in unrealistic entropy changes in the system for each transition[35].

Girshberg and Yacoby[36] proposed different model that combines both the displacive and order-disorder models. For the ferroelectric phase transitions, this explains the mode softening near them, and under application with BTO, was found to explain the over damping of the soft mode[37].

2.3 Domains and Domain Walls

During the paraelectric to ferroelectric phase transition, the anisotropic displacements of the Ti and O ions distort the Ti-0_6 octahedra in the cubic structure of BTO. The stretched edge becomes a tetrad z-axis of T BTO and is now the optic axis of the crystal. Further distortion leads to the formation of dipoles which tend to align themselves parallel to the z-direction. This direction now becomes the direction of spontaneous polarisation, causing strains at points of the crystal which is not aligned with this polarisation. In order to attain a minimum energy state, different regions of the crystal will polarize in energy equivalent directions until uniformity is reached.

A domain is a continuous volume within the material, in which the polarisation axis is in a uniform orientation. If the domain contains the polarisation axis in its plane, it is denoted as an 'a' or 'b' domain, whereas if it is perpendicular to the plane, it is denoted as a 'c' domain, for example in figure 5. A domain wall is defined as the boundary between two domains, and the relative polarisation between the two domains. Examples include the 180° domain wall, and non-180° domains such as the 90° domains walls in tetragonal ferroelectrics.

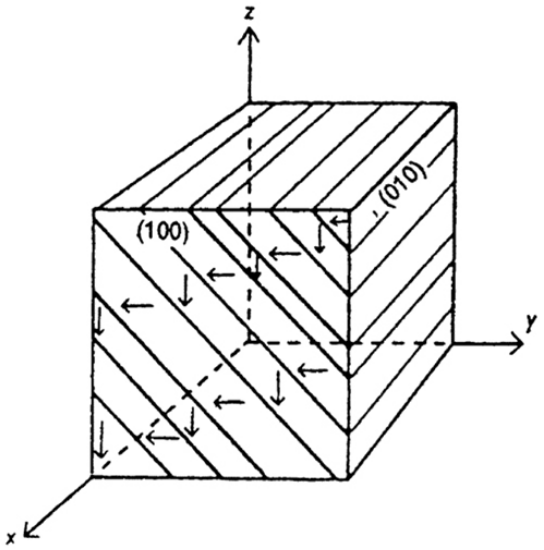

FIGURE 5 Diagram which shows the simply twinned crystals of $BaTiO_3$ and the mechanical twin boundaries. Short arrows indicate the c-direction of the individual components[38].

In reality, these definitions are not strictly followed, and rather are more of an exception as deviations from them are the norm. In tetragonal crystals, there are 6 orientations that the polarisation axis can follow, and these are parallel to three orthogonal directions possible for the crystal's c-axis[39]. Each domains polarisation is defined by one of these orientations. 90° domain walls are the $\{101\}$ crystallographic plane with orthogonal polarisation directions in a T structure. 180° domain walls separate domains with anti-parallel orientated polarisations.

Domain wall motion has a significant effect on ferroelectric properties in the physical sense. Structurally, by displacing atoms from their preferred positions to different positions, this results in what it called domain wall motion. This can be achieved through excitations caused by an externally applied electric force; high electric field amplitudes result in nucleation of new domain orientations, and at lower amplitudes, the occurrence of domain wall motion happens over short distances[39]. Further to this, domain wall motion has also been found to occur as a result of thermal effects[40].

2.4 Grain Boundaries

A grain boundary is the interface between two grains in a polycrystalline material of the same phase. They are defects in the crystal structure, for which study of these boundaries has been undertaken to study their effects on electromechanical and/or other properties[21].

To define a grain boundary, there needs to be 5 parameters mapping each of the macroscopic degrees of freedom shown in figure 6. To represent the misorientation in neighbouring grains, Euler angles, or an axis of rotation, and an angle of rotation are pair are used to describe boundaries. The result is that grain boundaries are described by two spherical angles for the normal plane relative to a crystal coordinate axis in one of the grains[41].

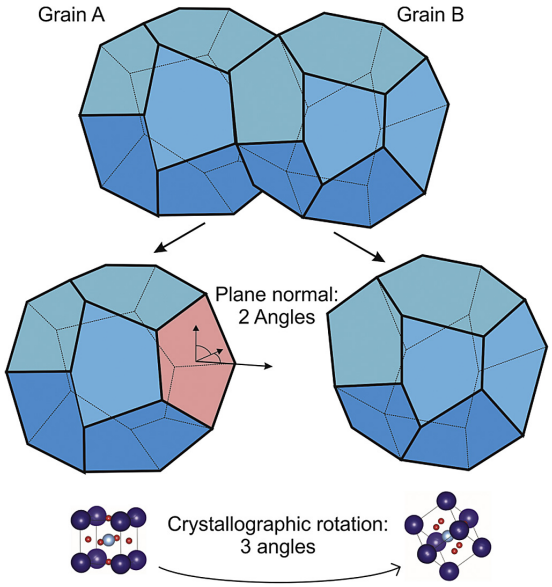

FIGURE 6 Diagram indicating the need for 5-dimensionality to describe a grain boundary. The grain boundary plane normal can be defined unambiguously by two angles with respect to the crystallographic orientation of Grain A. Using three angular parameters, they can be used to define the disorientation between the two grains and is shown by the rotated crystal structure[41].

That is to say there are three rotation angles producing the second grain, which is used in conjunction with two parameters to describe the boundary plane by its Miller indices of the other grain's coordinate system. Special grain boundaries are representation by the Σ value, which represents the misorientation between grains, e.g., $\Sigma = 3$ which is the grain boundary misorientation about the $\{111\}$ axis.

2.4.1 Twin Boundaries. Twin boundaries of crystals are the name given a special type of grain boundary, whereby the crystal structures either side of the grain boundary are symmetrical. These are called twin crystals and are important to not for applications of BTO as it can have a significant impact on its properties[38, 42–53].

Twin boundaries can form in a few ways. Such as during the growth process, known as growth twins, caused by defects or changes during growth, and can be contact twins or penetrations via the sharing of lattice points. They can be transformation twins whereby a pre-existing crystal undergoes a structural transformation due to varying temperature or pressure. New stable structures and symmetries that are formed during a transformation leads to an inter-growth of one or more crystals. Deformation twins are formed if a symmetrical arrangement is produced when the crystal bulk is physically disturbed[54].

One area of focus of BTO twin boundaries, and its effects on ferroelectric properties. In ferroelectric materials, there are two kinds of ferroelectric domains, 90 and 180°. They are what is described as mechanical twins and

are associated with the T phase[42, 43]. The 90° walls lie in the $\{101\}$ planes. The 180° walls lie on the $\{100\}$ planes[38]. The structural twins $\{111\}$ are formed during sintering of BTO, though it has been reported to grow at low temperatures through an adjustment of the process in synthesis stage[44], differ to these mechanical twins[44]. They are only observed in some grains, in particular, those with abnormal grain growths where it has been found to grow through boundary faceting[55], and can affect BTO's microstructure considerably[45]

2.4.2 Mechanical Twins. Twinning exists as a result of the low-temperature phase resulting in the coexistence of energetically degenerate variants[56] resulting in stress in the structure, thereafter the twinning has occurred, the stress in the structure reduces to a minimum[57]. In the two kinds of ferroelectric domains, 90° and 180° respectively, they are the mechanical twins that occur in the material when it is subjected to local stresses and internal imperfections, associated with the T phase and occur about the $\{101\}$ and $\{100\}$ planes[42, 43].

The 90° domains are formed by twinning on $\{011\}$, $\{01\bar{1}\}$, $\{101\}$, and $\{10\bar{1}\}$ planes and are the domain boundaries at which two domains are polarized at 90° to each other. Meanwhile the 180° domains can be formed by twinning when the $\{100\}$ or $\{101\}$ planes are domain boundaries between anti-parallel polarisation regions[58]. The 90° twins have two twinning structures as a result of domain wall charge. For a charge-neutral domain wall, the polarisations in each domain are almost perpendicular to each other and have a head-to-tail configuration. However, in the case of a charged domain wall, the domains are again perpendicular to each other but instead have head-to-head or tail-to-tail configurations[56]. The second twin of 90° however is unstable, and consequently it will undergo a transformation resulting in the formation of the first 90° twin with a zigzag twin boundary[59].

2.4.3 $\{111\}$ Structural Twins. The $\{111\}$ twins found are different to that of the mechanical twins, since they can be only be observed in some grains, particularly large grains, that exhibit abnormal grain growth[51, 55]. In fact, unlike most ferroelectric domains, the structural $\{111\}$ twins are unique to BTO[60]. It forms when in the twin plane, the stoichiometry of the structure building element differs to the parent structure. The $\{111\}$ twins are stable above and below the Curie temperature, even in cases where growth occurs and joins two free edges of a thin section in a single grain by a twin plane. The stability of the $\{111\}$ twins at high temperatures form hexagonal BTO, but the stability cannot be fully understood in some proposed models[61].

3 Methodology

This project is focused on the atomic structure of BTO, for its various phase transitions. Atomistic or force field-based techniques are important in evaluating the atomic structure of BTO. Further to this the inputted information, such as the interatomic potentials, and the structure of the phase is important to ensuring that the correct information is outputted. As a basis for the project, the goal is to reproduce the behaviour seen by BTO as it is subjected to a varying temperature range. This work currently is only dealing with the lattice dynamical properties of BTO, to the extent that a good foundation is made to then expand the simulations from the unit cell eventually to supercells which have the grain boundaries included, with latter focus on twin domains. Molecular dynamics can also be considered, and while do result in better reproductions of behaviour, it can also be far costlier than lattice dynamics.

Atoms are treated generally as point like particle, which have various interatomic potentials, which is then used to model particle interactions. However, this does not model these particles at the electronic level, such that many of the electronic properties of a material cannot be calculated. To counter this, force fields have been employed to accurately reproduce the structure of the atoms with accuracy[62, 63]. This work will be following suit employing GULP to perform these calculations[18].

3.1 Energy

For a majority of the calculations, one of the first the first simulation technique used is the calculation of the energy. Using the energy in the system allows a multitude of information to be gathered, starting off with the structure determination of BTO. The stability of the structure and its corresponding potentials is judged by the value of its energy, with decreasing energy insinuating greater stability.

In an ideal scenario, the simulation would incorporate all values of the structure, considering explicitly the position and momenta of electrons and nuclei to produce a value for internal energy. Practically however, this is not the case, so assumptions have to made to approximate the structure, which would result in simpler calculations to be done. In general, for an energy calculation, the energy of a system is calculated from a reference point, and the resulting change in energy is used to judge the stability. Assuming that the effects due to electrons can be merged into an effective atom, the change of energy in the system is often decomposed into an expansion in terms of interactions between different subsets within the total number of atoms, N:

$$E = \sum_{i=1}^{N} E_i + \frac{1}{2!}\sum_{i=1}^{N}\sum_{j=1}^{N} E_{ij} + \frac{1}{3!}\sum_{i=1}^{N}\sum_{j=1}^{N}\sum_{k=1}^{N} E_{ijk} + ...$$

where the first term, E_i represents the change in self energy of the atoms, the term E_{ij} representing the two-body interactions, the thirds term E_{ijk} representing the three-body and so on. Higher order terms become progressively smaller and thus negligible beyond a certain point, introducing a degree of parameterisation to compensate[18].

The self-energies of atoms are the result of atomic polarisation of due to external potential fields, where the two body terms are due to pairwise interactions between atoms such as the Coulomb interaction, and these depend on the particle distances between. Typically, three-body terms are based on bond angles, where an increase in energy is due to the size of the deviation from the ideal bond angle. In this project, up to the three-body potential is utilized despite the contribution generally getting smaller[64].

3.2 Two-body Long-Range Interaction - Coulomb Potential

When studying an ionic material, the Coulomb interaction is the most dominant term, so much so it contributes up to 90% of final total energy[18]. It is a two-body potential equation that models the electrostatic interaction between to particles that have a charge. It is given by Coulomb's law:

$$E_{ij}^{Coulomb} = \frac{q_i q_j}{4\pi\epsilon_0 r_{ij}}$$

where q is the charge of the ion, r_{ij} is the distance separating the two ions, i and j, and the constant ϵ_0 is the permittivitty of free space. Unlike a few other interactions, the Coulomb potential is a long-range interaction as it is inversely proportional to the distance between the ions.

3.3 Two-Body Short-Range Interactions

Contributions to the energy must include the interactions between atoms when they are bonded, or for ions that are in immediate coordination shells. These are known as the short-range interactions, with one such potential being the Buckingham potential:

$$E_{ij}^{Buckingham} = Ae^{(-\frac{r_{ij}}{\rho})} - \frac{C}{r_{ij}^6}$$

where A, ρ, and C are potential parameters. It is found that the radial decay of electron orbitals is exponential at reasonable distances, which is due to Pauli principle governing the interaction of repulsion between overlapping

electron densities. The second term in the equation is the attractive dispersion force due to the van der Waals force, which is caused between fluctuations in the dipoles on the two atoms. The first term must increase more rapidly than the second to ensure the two values of the term do not approach. As $r_{ij} \xrightarrow{0}$, the exponential term converges to a constant whereas the second term diverges. As a result, it becomes an increasingly attractive force, and one such method to overcoming this, is by also including the r^{-12} term.

Another short-range interatomic potential used was the Lennard Jones potential:

$$E_{ij}^{Lennard-Jones} = \frac{B}{r_{ij}^{12}} - \frac{C}{r_{ij}^{6}}$$

where B and C are parameters that are fitted to reproduce experimental properties. The second term is the same as the Buckingham potential. This potential differs with how it approaches modelling the Pauli repulsion, instead opting to structure the repulsion as the repulsion of the overlapping electron orbitals as opposed to the densities. Due to the form of this potential, with regards to the distance between the atoms, there will exist a distance in which the energy will be a minimum and the distances between the two atoms at equilibrium. As both of these two-body potentials are short range potentials, tending to zero for larger r, computationally one can apply appropriate radial cut-offs to the potentials, reducing computational cost without greatly impacting the calculation's accuracy.

3.4 Three-Body Interactions

Furthermore, the third term in the expansion of the energy term is utilized in this project for one of the potentials, and it is known as the three-body potential:

$$E_{ijk} = \frac{1}{2}k_2(\theta - \theta_0)^2$$

This represents the repulsion between bond pairs and occasionally lone pairs for a covalent perspective. The form chosen is usually a harmonic that penalises deviance from the expected angle for the crystal coordination environment.

3.5 Shell Model

The shell model has been used extensively in atomistic simulations of oxides, as the deformation of the electronic structure, or polarisability, can be phenomenologically described by this method[65]. It separates the individual ions within a material into to discrete point charges labelled as cores and shells, and they are linked together by a spring. The core represents the nucleus of an atom including tightly bound electrons, whereas the shell represents the center of a the more loosely bound outer ion electrons. The charge is split in such a way such that the total charge of the ion is the sum of the charge of the core and the shell. They are screened from each other, that is they are made not to interact with each other so that there is no electrostatic interaction between them, via the Coulomb force. The spring coupling the core to the shell is generally harmonic, which may or may not include higher order terms. Despite not interacting electrostatically with each other, they can both interact electrostatically with both the core and shell of other ions within the material. This is depicted in figure 7.

Typically, the short-range potentials that model the Pauli repulsion and the van der Waals forces are only applied to the shells, as the shells are a representation of the outer valence electrons. To model the bond between the atom core and the electron shell, it is the energy stored in a nonlinear spring due to the polarisation of the ion:

$$E_{cs}^{spring} = \frac{1}{2!}k_2\left|r_{ij}^2\right| + \frac{1}{4!}k_4\left|r_{ij}^4\right|$$

where r_{ij} is the core shell separation of an ion and k_2 and k_4 are the spring constants for the given species.

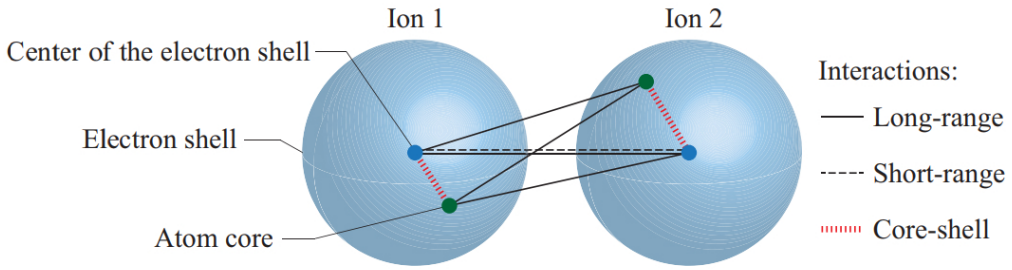

FIGURE 7 A diagram showing ions being split into cores and shells, and how they interact with each other via electrostatic interactions[66].

3.6 The Interatomic Potentials

The full libraries for each of the potentials used can be found in the appendix, see A.1 A.2, A.3, and A.4. Four potential libraries were chosen such that a more complete reproduction of the structure at differing phase transitions could be attained. One library of interatomic may perform better with a certain structure, but worse than others due the optimisation of the structure it was initially done for. 3 libraries were sourced which only utilized Buckingham potentials as their interatomic potentials, from Bush et al.[67], one as a culmination of three papers – two from both Lewis and Catlow[62, 63] and an independent paper from Catlow[68], one from a paper by Endres and Steinmann[66] (shorted to just Endres for readability when referenced). Another library was used which took a different approach to gathering the interatomic potentials, from Freeman et al.[69] whom performed fittings with multiple parameters to achieve a library which utilized three types of potentials, a combination of Buckingham, Lennard-Jones, and Three-Body potentials.

For the Endres library, two values for the spring constant was given: 31.0 ($||$) 101.27($\perp$), one seeming for the perpendicular spring constant and one for the parallel spring constant. With further consultation, there was no obvious way to incorporate both values using GULP into the library file for optimisation. It was mutually agreed upon the that the parallel value was to be taken for the library file.

Comparisons were then made for all the structural phase transitions of BTO for all libraries, as well as including the ternary oxides. thermodynamic responses were then studied for a range of temperatures to see how the BTO structures behaved for the different libraries in an attempt to see if one was better than the other.

3.7 Phase Structures

The structures for which the potentials are applied too are important, as starting from the correct structure proved to have a significant impact on the results of the data. Namely it required inputting the full unit cell as opposed to the primitive cell and implying symmetry, as optimisation runs would tend not to run and result in errors.

For all of the structures looked at, the full cell was inputted and the differences in parameters was studied. Further optimisation runs utilizing the previous iterations were also performed to see how or if the structure changed. The sources of the structures for orthorhombic, hexagonal, cubic, BaO and TiO_2 were from Wyckoff[70]. The tetragonal structure was from MaterialsProject[71], and the rhombohedral structure from Kwei et al.[72].

The main phase structures of BTO can be found in the appendices, shown here A.5, A.6, A.7, A.8.

3.8 Local Optimisation

This project focus on optimising the structures at different phases for the various interatomic potentials, with the goal of find the lowest energy of each structure which each set of potentials. As the calculated energy depends on the

structure and atomic separation, through an iterative process of gradually relaxing the ion positions in small steps, different algorithms attempt to relax the structure of the material such that there is a gradual downhill step in the energy landscape. This is repeated until certain conditions of the algorithms are met, such as finding a minimum energy value. The algorithms employed in this project through GULP use a combination of functions, gradients and second derivatives to search the energy landscape via one-dimensional line searches.

There are also other approaches to perform optimisations, such as utilization of the BFGS update of an inverse hessian[73], which was used as it useful to small systems, or systems close to the harmonic region. In other cases where minimums found might not be the true minimum, the RFO method was employed to perform displacements through utilization of the eigenvectors, determining if there are any imaginary modes.

3.9 Keywords and Options for Optimisation

Optimisations before the inclusion of energy was performed without free energy, so optimised results are based on athermal environment with only internal energy.

Numerous optimisations were formed for the ferroelectric and paraelectric phases of BTO, with some runs only running with the internal energy, while others utilized free energy and the focusing on seeing how the structures fluctuate with temperature. A number of keywords were employed in an effort to obtain more accurate reproductions of the structure. In most cases the standard file looked like the one exhibited in the appendix, B.

When performing optimisation runs many of the hashed-out options were tried in a bid to optimise the structure when it fails. In most circumstances the maximise number of cycles was greatly limited to 20 to be able to get a final structure without waiting a very large amount of time. However, this means that the structure wasn't allowed to optimise if it ever did, which in most cases it didn't. Due to what is most likely soft modes, the number of modes in the optimised system was constantly fluctuating and never fully achieving a fully optimised structure. RFO optimisations occasionally solved some of those issues, but even then, it might still eventually breakdown. Transition_State did further improve on the overall well-being of the optimisation, however it did increase the cost of each optimisation, so a compromise was made. Further to that, the points at which it is not pertinent to use the keyword, and whether it is applicable to certain input structures.

4 Results

4.1 Cohesive Energies

To start off the analysis of the different interatomic potentials, simple optimisation runs were performed with each potential on every structure, with the initial and final cohesive energies studied, the results are shown in 1

The values produced by the Freeman potential for cubic, hexagonal, BaO and TiO_2 agree with those given in there paper[69], though the values seen using the Lewis-Catlow potentials are much higher than those given: $c - BaTi_3$ -160.02 eV vs -144.59 eV, $h - BaTiO_3$ -159.94 eV vs -144.78 eV, TiO_2 -127.64 eV vs -112.94 eV, and BaO -32.58 eV vs -31.36 eV. This is an early indicator that the library utilized to produce the Lewis-Catlow library has some inaccuracies in it. In all of the values produced here were consistently higher, which suggests that one or some of the values in the Lewis-Catlow are incorrectly producing a false minimum on the energy landscape. Looking at the discrepancies in the results, there are noticeable differences in the cohesive energies values for the structures containing Ti ions. As the difference for BaO was much smaller as opposed to the other structures, it indicates that the discrepancy may be caused by one of the parameters to the titanium ion.

Comparing the other libraries to each other now, using the Freeman library results as a baseline, it is shown that it has the lowest minimum energy for all structures, a promising start for its use in lattice dynamics. Not too far off the energy values of the Freeman library is the Endres library, which while might not have found the true minimum energy of the system, is the closest to the Freeman library. (With that being said, taking into account the values produced

Table 1: Comparison of the cohesive energies of different lattice structures before and after optimisation using the different potentials.

		Potentials			
Structure	Energy /eV	Freeman	Endres	Bush	Lewis-Catlow
BaO	Before	-32.35353425	-24.99958024	-32.31435733	-31.32985366
	After	-32.58043205	-25.05083768	-32.36303249	-31.35915257
BaTiO3-c	Before	-160.0227428	-110.4741038	-154.4195951	-144.4883481
	After	-160.0239735	-110.5912729	-154.5831715	-144.5870618
BaTiO3-h	Before	-158.7367158	-110.0641790	-154.2892285	-143.7540703
	After	-159.8672440	-111.0340469	-156.0210140	-144.7790680
BaTiO3-o	Before	-159.3003568	-110.2790589	-154.3887768	-144.3752300
	After	-160.0239754	-110.5912730	-157.0325589	-144.6752130
BaTiO3-r	Before	-158.3352603	-110.0089633	-154.3395646	-144.2598549
	After	-160.0239736	-110.5912723	-156.7104719	-144.6279127
BaTiO3-t	Before	-159.6927786	-110.2579437	-154.0995590	-144.4086848
	After	-160.0239735	-110.5912729	-156.5155002	-145.0888820
TiO2	Before	-127.1884664	-86.46771055	-121.1995134	-112.5234288
	After	-127.6403537	-87.03633420	-122.7031907	-112.9434488

by Freeman et al.[69], the Lewis-Catlow library would be performing better optimisations than the Bush library). Interestingly the Endres library seems to have a minimum much higher than all of the other energies produced by other libraries. This could lead back to the fact that there were both perpendicular and parallel spring constants listed, but when trying either value produced similar results. It may imply that there is a way to utilize both spring constants on the same time to reproduce accurate energies. If not, it could be further implied that this library file just isn't suitable for use of lattice dynamics in GULP.

4.2 Lattice Parameter - Simple Optimisation Run

Next the lattice parameters for the starting structure and final optimized structure for each potential for each different structural phase is shown in table 2. The initial values for all the structures are taken from literature. Upon performing an optimisation run, all the lattice parameters for each structure changed. Universally the lattice parameters for the BaO structure increased by a fair amount, which would indicate that the source value might need to be verified to see if it is correct, or if there is a more accurate starting structure. The cubic phase undergoes both increases and decreases depending on the library used. A small reduction for most of the libraries except for the Lewis-Catlow library, which would again imply that this library has a mistake in it. Attempts to update and amend the library was attempted without much progress, and without further knowledge of the weak point causing it, it may be a systematic human error during the library construction. (The library is listed in the appendices for retroactive fixing.)

For the cubic, hexagonal, and orthorhombic structures, there isn't too much to report other than slight fluctuations in the lattice parameters, with the Freeman library tending to be closest to the initial starting structure. For the orthorhombic phase for the Bush library however, the lattice parameters for all directions changes quite significantly, with the distances between each parameter increasing. The library remains an outlier in this case, which suggest that it might not be suitable for accurately modelling the orthorhombic structure.

Moving onto the rhombohedral structure, it is again seen that there is a large fluctuation between the lattice parameters when the Bush library is used. Again, this implies that the parameters found in this library set aren't

Table 2: Comparison of the lattice parameters a, c, of different lattice structures before and after optimisation using the different potentials

			Potentials			
Structure	Latt. Param. /Å	Initial Start	Freeman	Endres	Bush	Lewis-Catlow
BaO	a	3.50000	5.33018	5.46124	5.49492	5.50751
	c	3.50000	5.33022	5.46124	5.49492	5.50751
BaTiO3-c	a	4.01180	4.00634	3.94389	3.93666	4.07938
	c	4.01180	4.00634	3.94389	3.93666	4.07938
BaTiO3-h	a	5.73500	5.79303	5.72019	5.69513	5.88732
	c	14.05000	14.21257	13.81563	13.72333	14.27475
BaTiO3-o	a	3.99000	4.00634	3.94390	3.38081	3.91669
	b	5.66900	5.66581	5.57752	7.28753	6.05332
	c	5.68200	5.66581	5.57748	6.74252	6.13532
BaTiO3-r	a	4.00360	4.00634	3.94389	3.43273	4.12119
	c	4.00360	4.00634	3.94389	4.91235	4.12119
BaTiO3-t	a	3.99470	4.00634	3.94389	3.62760	3.78700
	c	4.03360	4.00634	3.94390	5.35576	5.35381
TiO2	a	4.59400	4.48855	4.30928	8.08376	4.46962
	c	2.95900	3.14343	3.00752	2.70547	3.20098

suited for the low temperature ferroelectric phases of BTO. This could be due to how the library parameters were initially created and may have instead have opted to choose parameters that optimise better for the higher temperature structures.

The tetragonal phase provides some interesting results too. In the case of the Freeman library, it is found that there is no longer a difference in the lattice parameters a and c, and when the Freeman library is used, it forces the structure to cubic. This is similarly the case for Endres library too, which also goes from having a tetragonal structure to cubic. Interestingly the Bush and Lewis-Catlow libraries still maintain a difference between the lattice parameters, but the difference has greatly increased and is no longer an accurate representation of the tetragonal phase. That being mentioned, it should be noted that these optimisations were performed athermally with the internal energy, so structures which only exist at higher temperatures may not be accurate.

Finally looking at the TiO_2 ternary oxide, the only result which is striking is the value produced by the Bush library where the value for the lattice parameter has nearly doubled. Looking at the outputted file, it appears to by the oxygen ions in the structure, in which the shell undergoes rigorous changes to its position relative to its starting position. The oxygen ions in the ternary structure might be influenced greatly by electrostatic contributions from other shells or perhaps its own core oxygens, hinting that potentially the spring constants for oxygens my not be correct.

4.3 Ti-O Bond Lengths

Next an in-depth look at how the Ti-O bond distance fluctuates with structure and interatomic potentials, shown in table 3. The hexagonal structure shows how the differing interatomic potentials interact with the Ti-O bonds, with the starting structure having symmetry between the distances, this is lost upon optimisation. For the Freeman potentials, all symmetry is lost completely, similarly true for the Endres potentials. Bush and the Lewis-Catlow potentials maintain the symmetry for the Ti1-core O2-core/shell distances, with the distances being equal for both. For the other distances, Endres potentials follow the trend set by the staring structure, but the distances but the distances between the

oxygen ions and the Ti2 ions fluctuate slightly. The Lewis-Catlow potentials maintain both the trend and symmetry of the initial starting structure. For the cubic structure the bond distances undergo small fluctuations because of changing libraries, nothing unexpected in the results as the distances between the core and the shell remain equal.

Table 3: Comparison of the Ti-O bond lengths varying with potentials.

						Potentials			
						Distance /Å			
Structure	Atom 1		Atom 2		No. Bonds	Before	Freeman	Endres	Bush	Lewis-Catlow
Hexa	Ti1	core	O2	core	6	1.9478	1.9831	1.9623	1.9555	2.0356
			O2	shell	6	1.9478	2.0019	1.9604	1.9555	2.0356
	Ti2	core	O1	core	3	1.9613	2.1400	2.0014	1.9183	1.9261
			O2	core	3	2.0153	1.9895	1.9891	1.9801	1.9946
			O1	shell	3	1.9613	1.9866	1.8549	1.7673	1.9261
			O2	shell	3	2.0153	1.9712	1.9909	1.9789	1.9946
Cubic	Ti	core	O	core	6	2.0059	2.0032	1.9719	1.9683	2.0397
			O	shell	6	2.0059	2.0032	1.9719	1.9683	2.0397
Tetra	Ti	core	O1	core	1	1.8209	2.0032	1.9718	1.7818	1.5990
			O1	core	1	2.3951	2.0032	1.9721	3.5740	3.7548
			O2	core	4	2.0107	2.0032	1.9719	1.8939	1.9628
			O1	shell	1	1.8209	2.0032	1.9717	1.5805	1.5990
			O1	shell	1	2.3951	2.0032	1.9722	3.7753	3.7548
			O2	shell	4	2.0107	2.0032	1.9719	1.8770	1.9628
Ortho	Ti	core	O1	core	2	1.9982	2.0032	1.9719	1.9199	2.0015
			O2	core	2	1.9038	2.0032	1.9720	1.9199	1.6241
			O2	core	2	2.1126	2.0032	1.9720	1.7445	2.7128
			O1	shell	2	1.9982	2.0032	1.9719	1.8020	2.0015
			O2	shell	2	1.9038	2.0032	1.9719	3.3150	1.6241
			O2	shell	2	2.1126	2.0032	1.9720	3.6717	2.7128
Rhombo	Ti	core	O	core	1	1.8776	2.0032	1.9719	1.7726	1.7717
			O	core	1	1.8776	2.0032	1.9719	1.7730	1.7717
			O	core	1	1.8776	2.0032	1.9719	1.9068	1.7717
			O	core	1	2.1351	2.0032	1.9719	1.9073	2.3709
			O	core	1	2.1351	2.0032	1.9719	3.2304	2.3709
			O	core	1	2.1351	2.0032	1.9719	3.2422	2.3709
			O	shell	1	1.8776	2.0032	1.9719	1.5332	1.7717
			O	shell	1	1.8776	2.0032	1.9719	1.5332	1.7717
			O	shell	1	1.8776	2.0032	1.9719	1.8482	1.7717
			O	shell	1	2.1351	2.0032	1.9719	1.8493	2.3709
			O	shell	1	2.1351	2.0032	1.9719	3.4715	2.3709
			O	shell	1	2.1351	2.0032	1.9719	3.4826	2.3709

Moving on to the latter structures, the real differences between the potentials can be seen. For all the structures, the Freeman potentials for all Ti-O bond distances revert to the same value of 2.0032 /°A. In comparison to the other potentials, all the distances have some fluctuations to some degree, with the Bush and Lewis-Catlow potentials having

quite significant fluctuations, meanwhile the Endres potentials have a relatively smaller fluctuation and are close to having the same distances for each structure, (and equal in the case for the rhombohedral structure). The cause of this difference is most likely due to the fact that the Freeman potentials use a three-body potential and eliminate the Ti shell during optimisations. As a result, the effect of this is the distances of Ti-O bonds no long vary for the structures and become equidistant. This may have ramifications of the ability to accurately all the different structural phases of BTO. The Endres potentials behave similarly to the Freeman potentials but aren't as completely rigid as it does have some variation. This suggests that exclusively using Buckingham potentials might yield similar results to experimental, but not as accurately as those potentials proposed by Freeman.

The Bush and Lewis-Catlow again follow the trends of the initial starting structures, in terms of the relative Ti-O bond distances to each other, however, the distances have significantly changed, resulting in more extreme differences in the distances for the different Ti-O bonds. This suggests that there is a clear divide between the Freeman and Endres potentials, with the Bush and Lewis-Catlow potentials.

4.4 Dispersion Curves and Density of States

Next the vibrational properties of the different phase structures were studied via phonon dispersion curves and density of states. Simulations were run on an unoptimised structure to get an initial graph, the structure was then optimised, then a single run was carried out on the new optimised structure then directly compared to the original. These were all performed using the internal energy. The unstable modes, soft phonons, are associated to a negative curvature of the energy hypersurface, and whose corresponding eigenvectors have imaginary frequencies[74].

4.4.1 Cubic Structure, Pm3m. The calculated phonon dispersion curves for the cubic BTO structure are plotted along the high symmetry directions in figure 8, the points of symmetry are $\Gamma = (0.0, 0.0, 0.0), X = (0.0, 0.5, 0.0), M = (0.5, 0.5, 0.0), R = (0.5, 0.5, 0.5)$.

The dispersion curves for the starting structures have no soft modes except for the Endres potentials, suggesting that the values used result in the initial structure being unstable. The optimised structure for the Lewis-Catlow potentials matches Ghosez et al. in their paper[74], implying that these potentials accurately describe the soft modes, whereas every other potential only result in the real frequencies. The density of states for the Bush potentials have broad input peaks as opposed to other potentials and the optimised peaks. Not shown in the graphs are some very low- and high-frequency bands, which appear to be periodic in nature, it is not sure what exactly what this describes other than it being very unstable, but an example can be seen in appendix 22.

The freeman potentials shown very little change between the unoptimised and optimised structure. It does provide the expected cubic structure of BTO, despite not containing any soft modes, which also allows the optimisation to run smoothly without the number of modes changing. The Lewis-Catlow potentials have a somewhat evenly distributed amount of frequencies, with neither end of the spectrum having higher intensity. The Endres potentials differ to that in that there is a higher weight towards the lower end of the frequencies, with much large intensities as opposed to the high-frequency end. Further to that, the Freeman potentials appear to have a band gap in the frequencies around 500cm^{-1}, for both the unoptimised and optimised structure.

4.4.2 Tetragonal Structure, P4mm. The calculated phonon dispersion curves for the cubic BTO structure are plotted along the high symmetry directions in figure 9, the points of symmetry are $\Gamma = (0.0, 0.0, 0.0), X = (0.5, 0.0, 0.0), M = (0.5, 0.5, 0.0), Z = (0.0, 0.0, 0.0), R = (0.5, 0.0, 0.5), A = (0.5, 0.5, 0.5)$.

Similar behaviour for the Bush potentials in regard to very large low- and high-frequency bands for the input structure, and a broad density of states as a result of it. For the other potentials the behave similarly in how the starting input structure has some soft modes for the input structure but contains only real frequencies once it has undergone optimisation.

Just like the cubic structure the Lewis-Catlow potentials result in an even distribution of vibrational frequencies, with the Endres potential favouring the lower end, and the Freeman potential once again producing a band gap. Upon further inspection, it can be seen that the optimised structure for tetragonal is the same as that seen for the cubic structure.

4.4.3 Orthogonal Structure, Amm2. The calculated phonon dispersion curves for the cubic BTO structure are plotted along the high symmetry directions in figure 10, the points of symmetry are $\Gamma = (0.0, 0.0, 0.0), S = (0.0, 0.5, 0.0), R = (0.0, 0.5, 0.5), Z = (0.0, 0.0, 0.5), Y = (0.5, 0.5, 0.0), T = (0.5, 0.5, 0.5)$.

Onto the orthogonal structure, the Endres potential produces soft modes for the unoptimised structure, meanwhile the Lewis-Catlow produces them for the optimised structure. The bush potential shows an imaginary frequency along the $\Gamma - S$ line, as well as extreme low- and high-frequencies bands which are not pictured.

The Freeman potential has both structures without any imaginary modes and indicates that the optimised structure has shifted the lower and middle frequencies up, whereas for the high-frequency phones it has been shifted down. The density of states again follows a similar trend, but it isn't as defined as the cubic and tetragonal structures. The Lewis-Catlow potentials see a general shift down in in frequency while there is an increase in frequency for the Endres potentials.

4.4.4 Rhombohedral Structure, R3m. The calculated phonon dispersion curves for the cubic BTO structure are plotted along the high symmetry directions in figure 11, the points of symmetry are $\Gamma = (0.0, 0.0, 0.0), L = (0.0, 0.0, 0.5), Z = (0.5, 0.5, 0.5), F = (0.5, 0.5, 0.0)$.

For the Bush potentials, its behaviour is more in line with the others, in which there isn't any extreme low- or high-frequencies. Instead it treats the initial structure as having no imaginary modes, with the final structure have two imaginary frequencies, one along the $L - Z$ line, and another along the $Z - R$ line. The density of states after optimisation do not peak as high as the before state, bus has spread out more in frequency at both ends of the spectrum.

Lewis-Catlow potentials have shifted frequencies in the mid and upper range, but now has soft modes that run between all the points of high-symmetry in the Brillouin zone. This sentiment was countered with the Endres potentials, where there are small shifts in frequency and intensity, but the soft mode in the initial structure does not appear in the final structure.

Results of the Freeman optimisation counter these, showcasing that the initial structure contained soft modes, but that the final optimised structure does not. For the rhombohedral case, the band gap seen in the density of states is wider than those seen for the other structures. The Endres potentials contains the least high frequency information as opposed to the others.

Two of the final structures using the Bush potentials, the tetragonal and the rhombohedral phase, contain imaginary modes after optimisation. Moreover, the Catlow potentials resulted in soft modes for three of the phases. These juxtapose with the Endres and Freeman potentials, in which all of the final structures did not contain any soft modes.

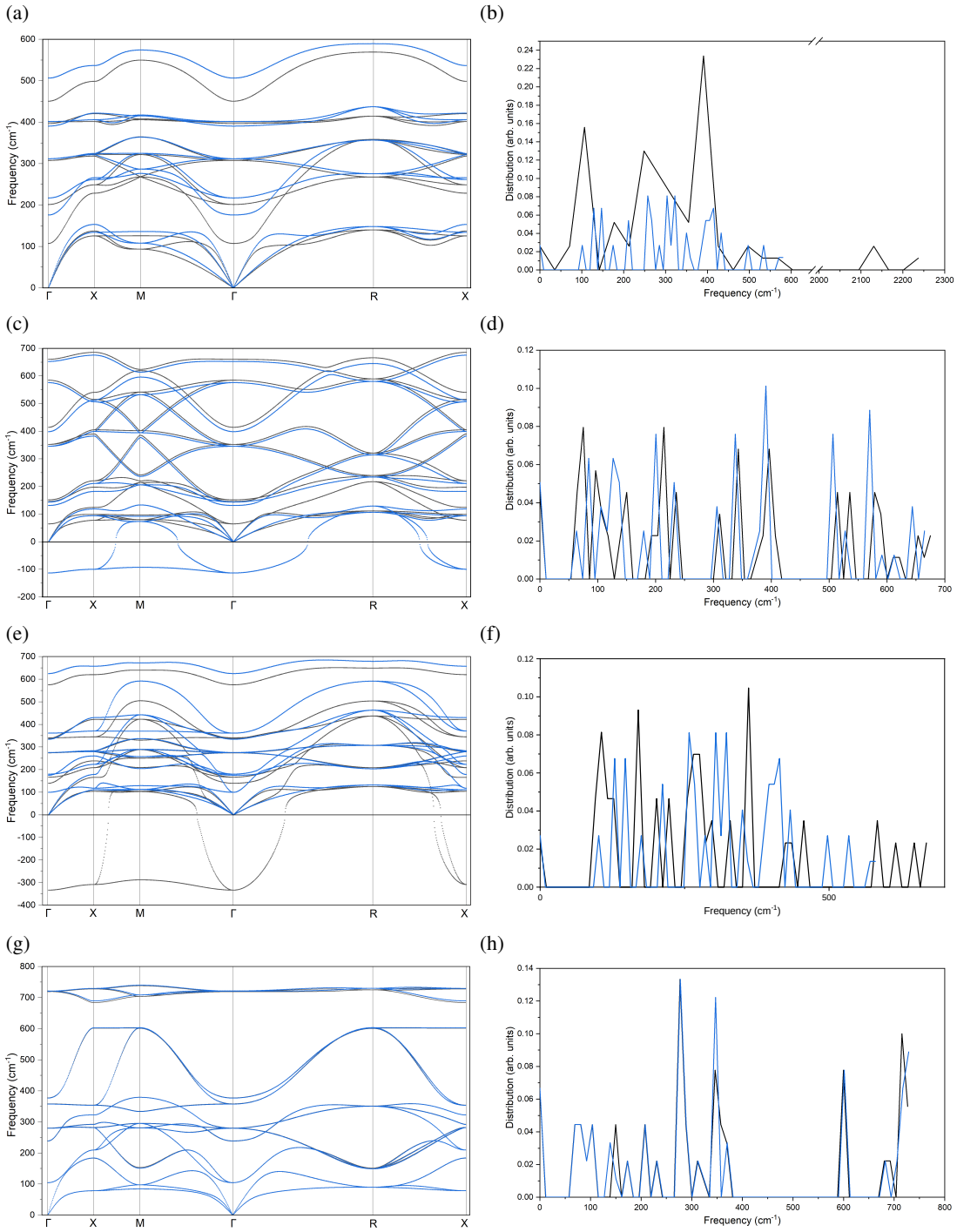

FIGURE 8 Information about the vibrational properties of the cubic BTO structure, detailing the dispersion curves for (a), (c), (e), and (g), and the corresponding density of states (b), (d), (f), and (h) for the different potentials Bush, Lewis-Catlow, Endres, and Freeman respectively. The black lines indicate the points in the unoptimised structure, and the blue representing the optimised structure.

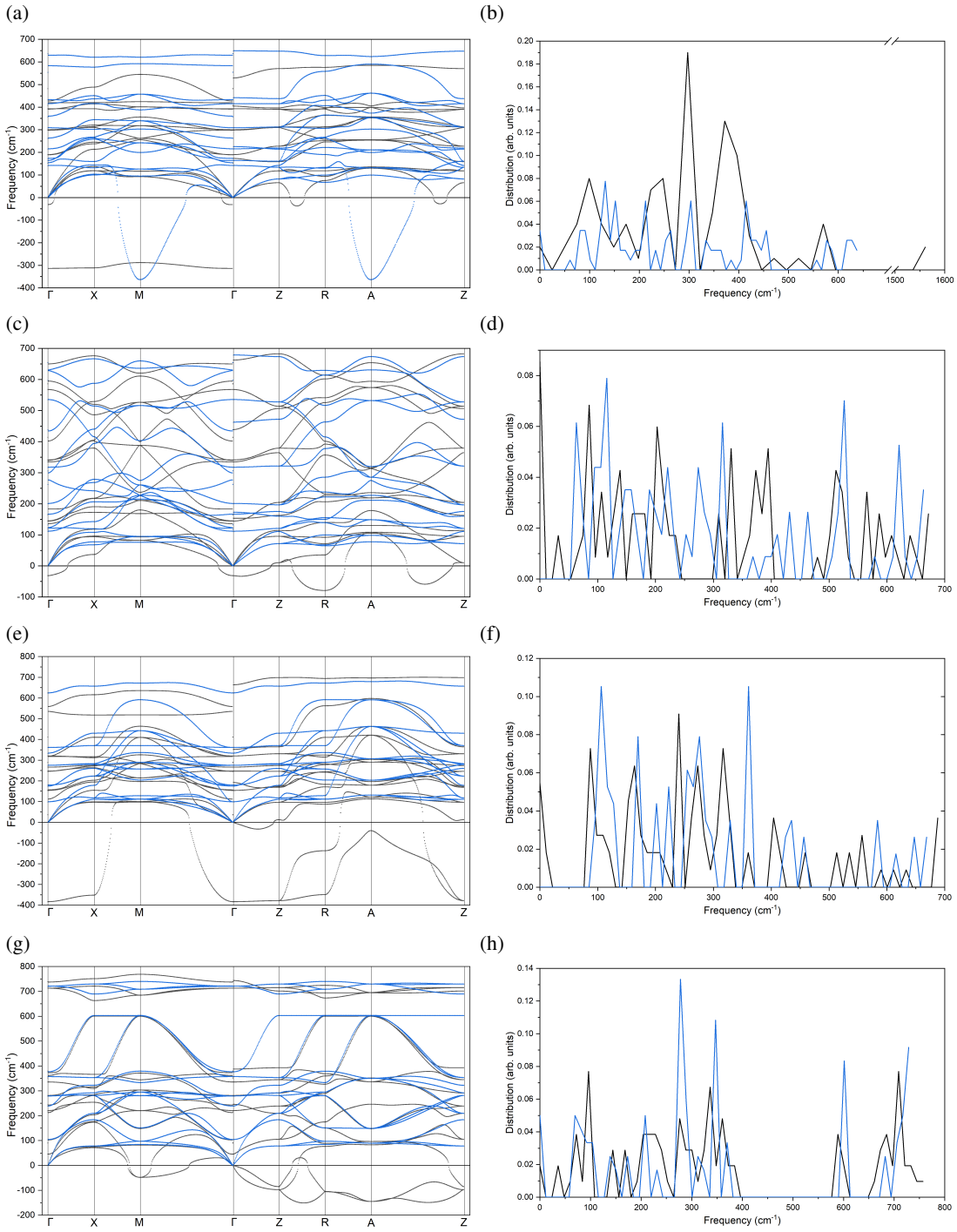

FIGURE 9 Information about the vibrational properties of the tetragonal BTO structure, detailing the dispersion curves for (a), (c), (e), and (g), and the corresponding density of states (b), (d), (f), and (h) for the different potentials Bush, Lewis-Catlow, Endres, and Freeman respectively. The black lines indicate the points in the unoptimised structure, and the blue representing the optimised structure.

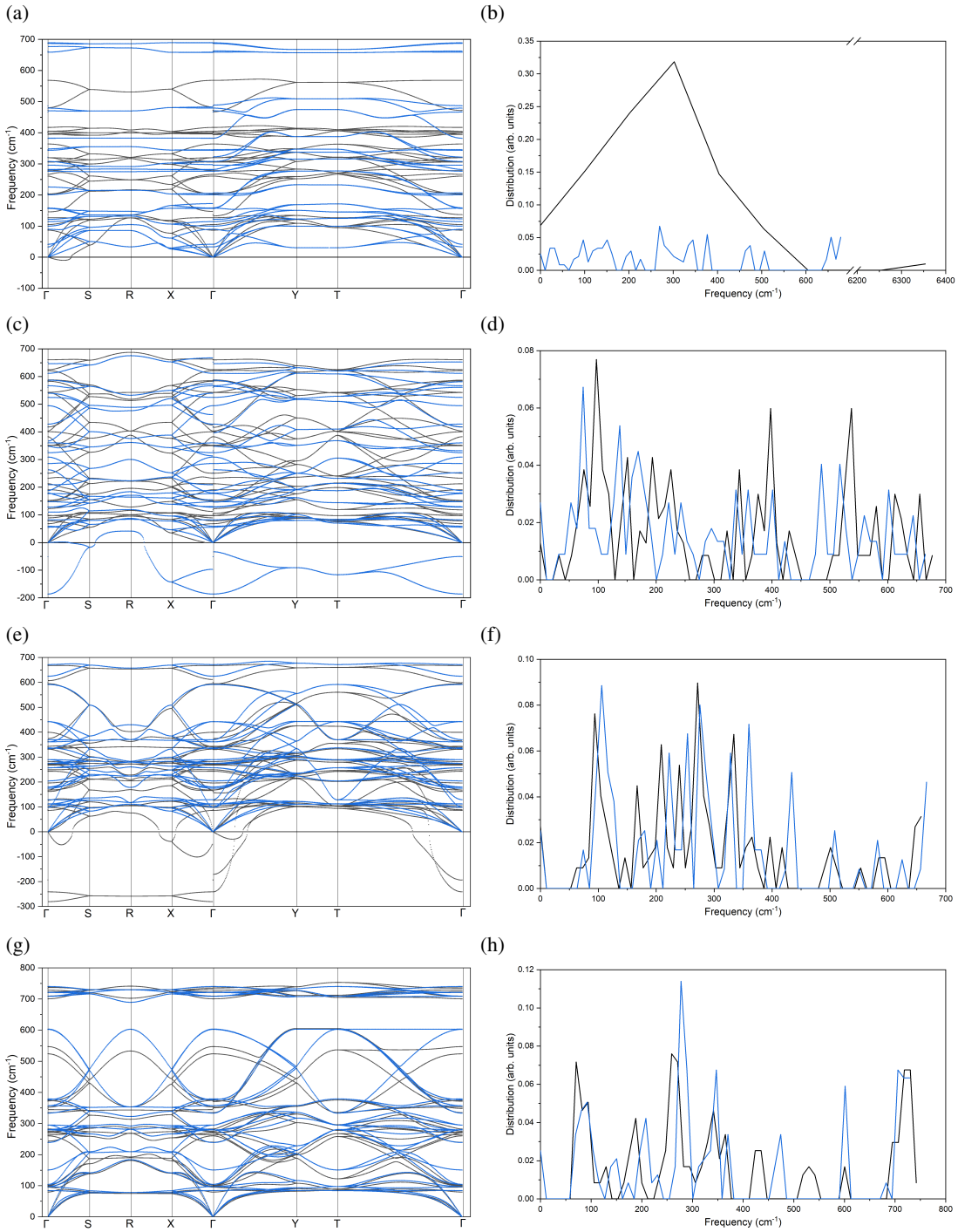

FIGURE 10 Information about the vibrational properties of the orthogonal BTO structure, detailing the dispersion curves for (a), (c), (e), and (g), and the corresponding density of states (b), (d), (f), and (h) for the different potentials Bush, Lewis-Catlow, Endres, and Freeman respectively. The black lines indicate the points in the unoptimised structure, and the blue representing the optimised structure.

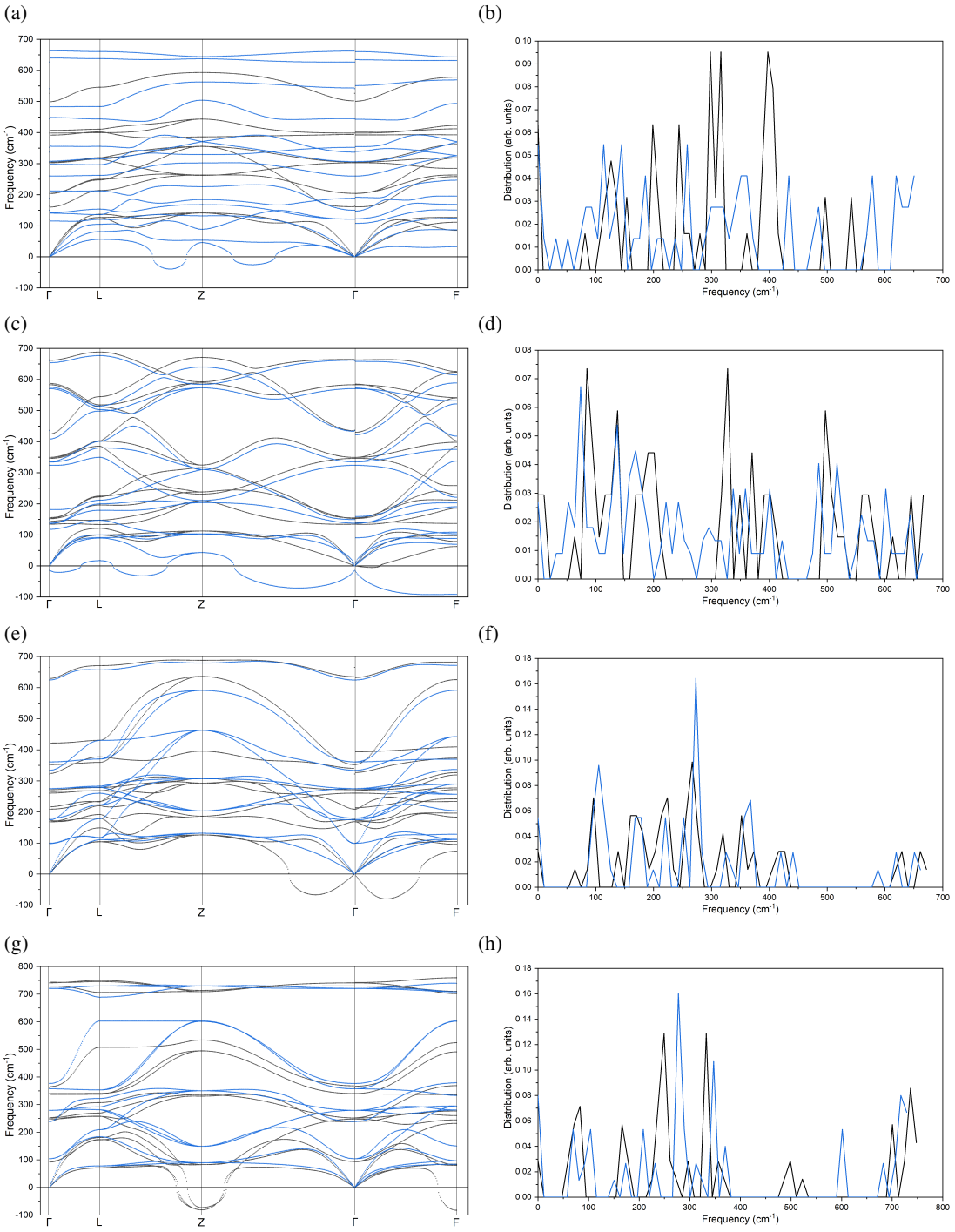

FIGURE 11 Information about the vibrational properties of the rhombohedral BTO structure, detailing the dispersion curves for (a), (c), (e), and (g), and the corresponding density of states (b), (d), (f), and (h) for the different potentials Bush, Lewis-Catlow, Endres, and Freeman respectively. The black lines indicate the points in the unoptimised structure, and the blue representing the optimised structure.

4.5 Verifying with Shrinking Factor

Shrinking factors were applied to the cubic phase structure and were run for a range of increasing temperatures to study how the potentials handled and an increasing factor, and whether some performed better than others.

4.5.1 Bush Potential. For the Bush potential, it performed well and described the structure expected quite uniformly, depicted it figure 12. A shrinking factor of two was enough for the lattice parameters and free energy to converge to an acceptable level. For future temperature range runs, a shrinking factor of two was chosen as it provided acceptable results with a good computational time too.

4.5.2 Lewis and Catlow Potential. The results were messier for the Lewis-Catlow potential, seen in figure 13. For the shrinking factor 1, the lattice parameters behaved uniformly at lower temperatures, but for increasingly larger temperatures, there was a lot of variation between the a and c parameters. Similarly, the free energy for the 1x1x1 shrinking factor fluctuating and jumped throughout the temperature range.

For a shrinking factor of two, it appeared to calm down, with lattices parameters a and c having equal values for the temperature range. The free energies were also more stable and followed and uniform descent as the temperature increased. Interestingly, as the shrinking factor increased, things once again began to get quite disorganized. At around 650K, up until this point the lattice parameters were equal, they suddenly began to change at the higher temperatures, splitting in size and no longer following the same path. Small jumps in the free energy were also noted as early on as 200K.

As the factor increased to 4, the point in which the lattice parameters would no longer follow the same trajectory occurred at a lower temperature this time of 400K. After this point they were no longer equal, but the difference between the two was not as great as for the previous shrinking factor. Whether this has any correlation to the transition temperature remains to be seen, as 400K is the tetragonal-cubic phase transition. This is also reflected in the computational time, where shrinking factors 3 and 4 saw noticeable jumps at the 600K and 200K mark respectively.

4.5.3 Endres Potential. For the Endres potential, figure 14 shows it too also had an interesting progression as the shrinking factor was increased. For a factor of 1, the lattice parameters and free energy were mostly uniform except from a small jump at the 300K mark, where there was a brief discrepancy in the lattice parameters. For a shrinking factor of 2, things further improved, with a coherent lattice parameter throughout the range, and a lower free energy range.

Upon increasing the shrinking factor even more, again like the Bush potentials some displacements were introduced. For the shrinking factor 3, as it approached 600K, the values became unstable and different to each other, as well as both increasing in magnitude. For 4x4x4 the split occurred earlier at 400K and increased even earlier at 300K. For the free energies, the shrinking factors 3 and 4 increased in magnitude as it approached the higher temperatures as compared to the 2x2x2 factor. Computational time was tiered as expected, but unlike the Lewis-Catlow potentials, the jump in computational time was not as great.

4.5.4 Freeman Potential. Finally, looking at the Freeman potential in figure 15, the results are more uniform for every factor. The lattice parameters converge at a shrinking factor of 3, and the free energies at a factor of 2. Unusually, the behaviour of the lattice parameters for a factor of 3 tended to decrease in size as opposed to increasing as seen for all other potentials and factors. For further calculations a shrinking factor of 2 was chosen to keep results consistent with the other potentials, and to also save on computational costs.

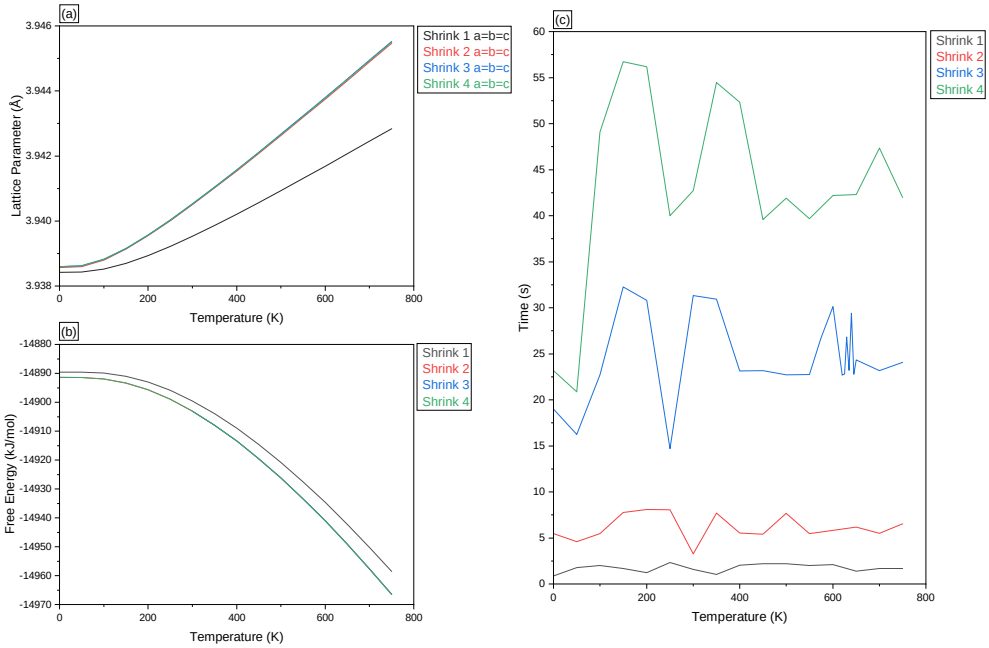

FIGURE 12 Detailing how the (a) lattice parameters, (b) free energy and (c) computational time vary as a resulting of increasing the shrinking parameters when using the Bush potentials

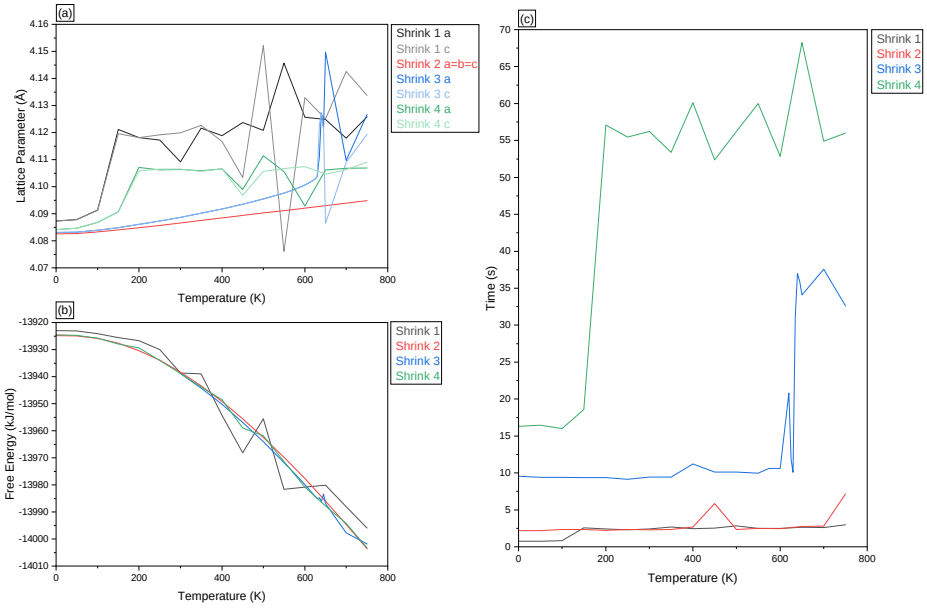

FIGURE 13 Detailing how the (a) lattice parameters, (b) free energy and (c) computational time vary as a resulting of increasing the shrinking parameters when using the Lewis-Catlow potentials

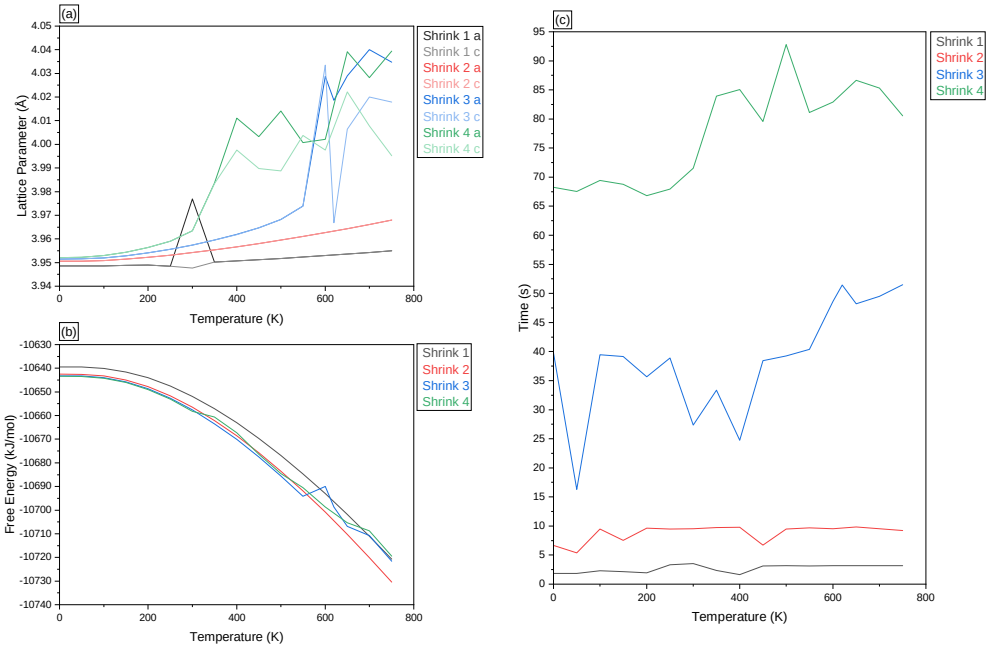

FIGURE 14 Detailing how the (a) lattice parameters, (b) free energy and (c) computational time vary as a resulting of increasing the shrinking parameters when using the Endres potentials

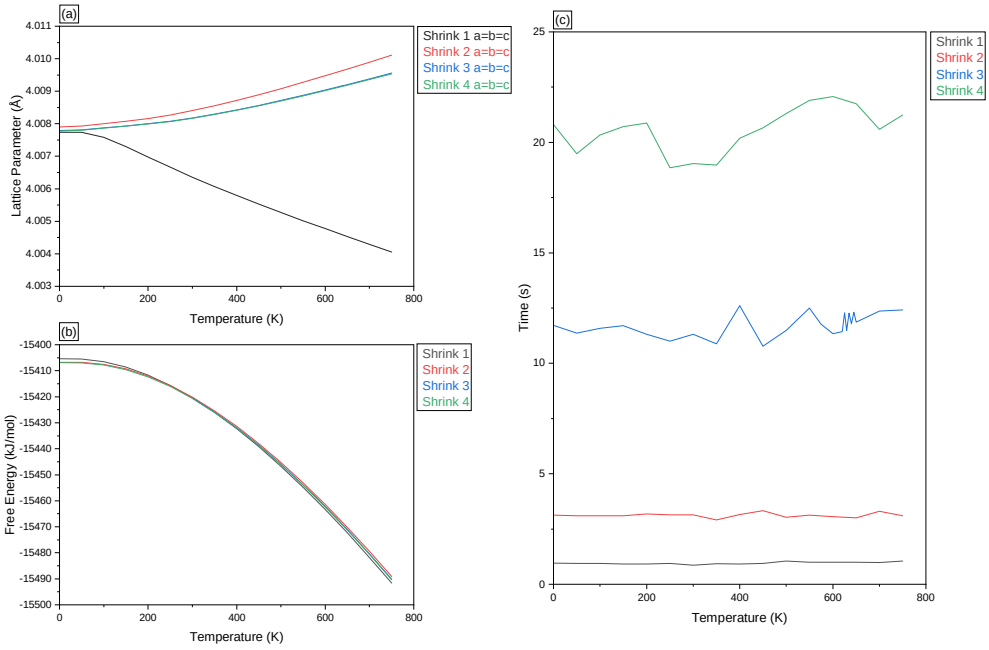

FIGURE 15 Detailing how the (a) lattice parameters, (b) free energy and (c) computational time vary as a resulting of increasing the shrinking parameters when using the Freeman potentials

4.6 Lattice Parameters

A shrinking factor of two was utilised for all runs throughout the temperature range of 0K to 750K, for each potential for every structure. The values for the lattice parameters will be compared to previous values found in literature: rhombohedral: $a = b = c =$ 4.004Å[72]; orthorhombic: $a =$ 3.984Å, $b =$ 5.674Å, $c =$ 5.692Å[72]; tetragonal: $a = b =$ 3.991Å, $c =$ 5.035Å[72]; cubic: $a = b = c =$ 4.011Å[26].

4.6.1 Bush Potential. Looking first at the Bush potential, the cubic structure behaves uniformly throughout the range, albeit with a value lower than experimental[26, 74]. The tetragonal structure is much more different than found experimentally, with an approximately c/a ratio of 1.47, this is not a true reproduction of the tetragonal structure. The stretch seen is nonphysical and appears to have no deviation as the temperature is varied; using the Bush potential for the tetragonal structures should therefore be avoided. The orthorhombic structure behaves somewhat as expected, however the values for the b and c parameters are much higher than seen experimentally[72], so it too is not a good representation of the orthorhombic structure. For the rhombohedral structure, it's behaving as one, but more as an orthorhombic structure interestingly, the cause of which isn't entirely obvious at this point. Looking at all the structures, it is inadvisable to use the bush potential to describe accurately any of the structural phases of BTO, as in some cases they're nonphysical or not the best representation.

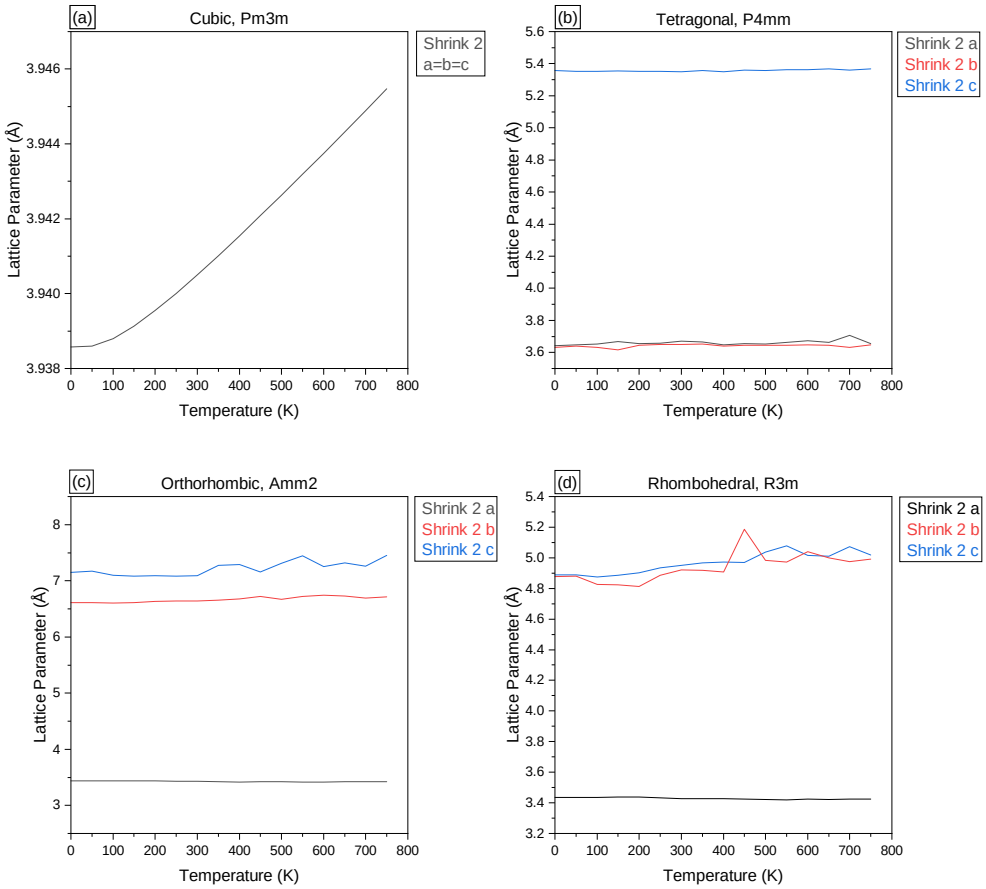

FIGURE 16 The fluctuation of the lattice parameter as a result of temperature, using the Bush potentials for (a) cubic structure, Pm3m (b) tetragonal structure, P4mm (c) orthorhombic structure, Amm2 and (d) rhombohedral structure, R3m.

4.6.2 Lewis and Catlow Potential. Moving onto the Lewis-Catlow potentials, the cubic structure behaves as expected, though the lattice parameters are slightly higher than what has been shown experimentally[26]. Looking now at the tetragonal structure, it too has lattice parameters much greater than expected just like the Bush potential. However, at approximately the transition temperatures, for rhombohedral to tetragonal at 283K and tetragonal to cubic at 400K, there is a substantial shift in both the a and c parameter. It is unsure whether this is indicative of a decent reproduction of the structure, as further refinements to the optimisation process would need to be done to verify that this is the actual progression of the structure with temperature. An optimisation run using the "Transition_State" keyword was performed and can be seen in appendix 23. Focusing on the orthorhombic structure, it behaves as intended, however it still has inflated lattice parameters, though to not the same extent as the Bush potentials. Finally, onto the rhombohedral structure, it can be seen that there is a lot of fluctuations for all of the lattice parameters in each direction. The general trend is that the parameters are similar on average, but they aren't very coherent as it increases in temperature. In the lower temperature range in which they would be used, the magnitudes are still much higher than expected.

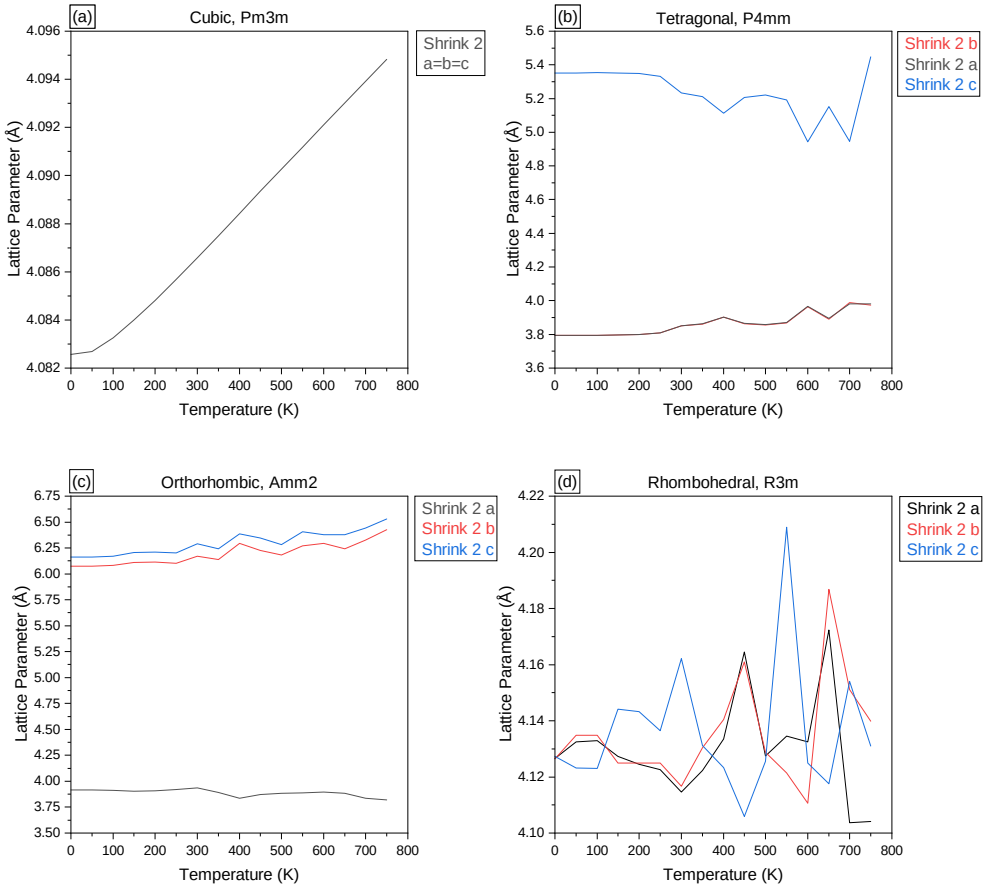

FIGURE 17 The fluctuation of the lattice parameter as a result of temperature, using the Lewis and Catlow potentials for (a) cubic structure, Pm3m (b) tetragonal structure, P4mm (c) orthorhombic structure, Amm2 and (d) rhombohedral structure, R3m.

4.6.3 Endres Potential. Looking at the lattice parameters given by the Endres potential, the cubic structure maintains uniformity through the temperature range, but the values given are slightly below what is experimentally seen. The tetragonal structure has values closer to what is expected, differing from the Bush and Lewis-Catlow

potentials in such that there isn't a clear split between the parameters. It does however have a lot of variance in the values, around 550K there is a noticeable split, with some smaller gaps at other points. This is due to the point at which the optimisations were stopped, it may be beneficial to repeat optimisation with either a larger maximum number of cycles or applying some additional keywords or options to modify the optimisation to result to achieve a more uniform progression.

Looking at the orthorhombic structure now, it is much more in line with what has been seen experimentally, with a, b, and c, lattice parameters in agreement[72]. The fluctuations with temperature are much smaller than the tetragonal or rhombohedral structure. Therefore, in the temperature range for use with the orthorhombic structure, the Endres potentials would be suitable to accurate portray the structure. Lastly studying the rhombohedral structure, once again there is a fair amount of variation in the values as the temperature increases. Comparing it to the Lewis-Catlow potential results, there is a much more visible uphill trend in the lattice parameter values, and the instability in those values aren't as great, the values themselves however are lower than what is expected.

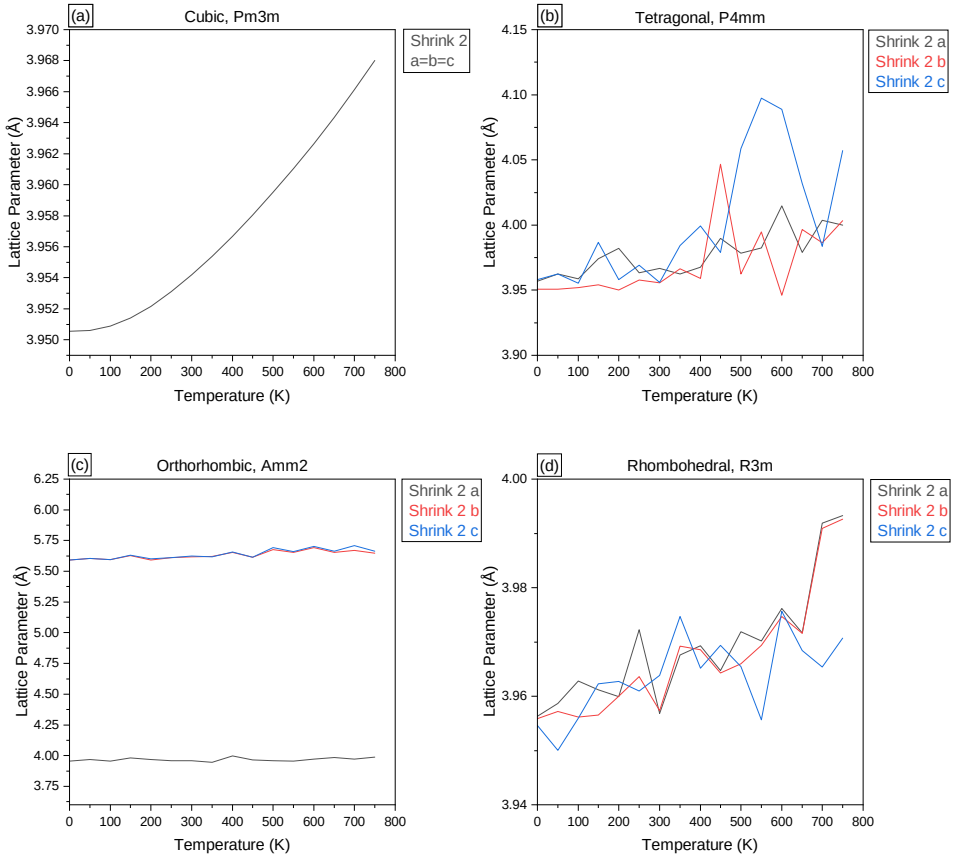

FIGURE 18 The fluctuation of the lattice parameter as a result of temperature, using the Endres potentials for (a) cubic structure, Pm3m (b) tetragonal structure, P4mm (c) orthorhombic structure, Amm2 and (d) rhombohedral structure, R3m.

4.6.4 Freeman Potential. Lastly, the structures utilising the Freeman potentials. Compared to the other three potentials, all of the structures have a much smoother progression for increasing temperature, and apart from the orthorhombic structure, increase in value with increasing temperature.

The cubic structure has values close to the expected but are all negatively displaced by 0.01 Å from experimental[26]. The tetragonal structure doesn't have the desired c/a ratio that is expected from BTO as the differences

between the a and c parameters an order of magnitude to small[72]. The orthorhombic structure sees no variation in lattice parameter values with temperature, although it does have the expected values in the temperature range in which this structure occurs. It agrees with the experimental values and is similar to the structure produced using the Endres potentials, just with no fluctuation with temperature. This implies that with these potentials, the orthorhombic structure does not rely on temperature. The tetragonal structure in the temperature range for this structure acts similarly to experimental, with only a slight splitting of lattice parameters where ideally all the values would be the same.

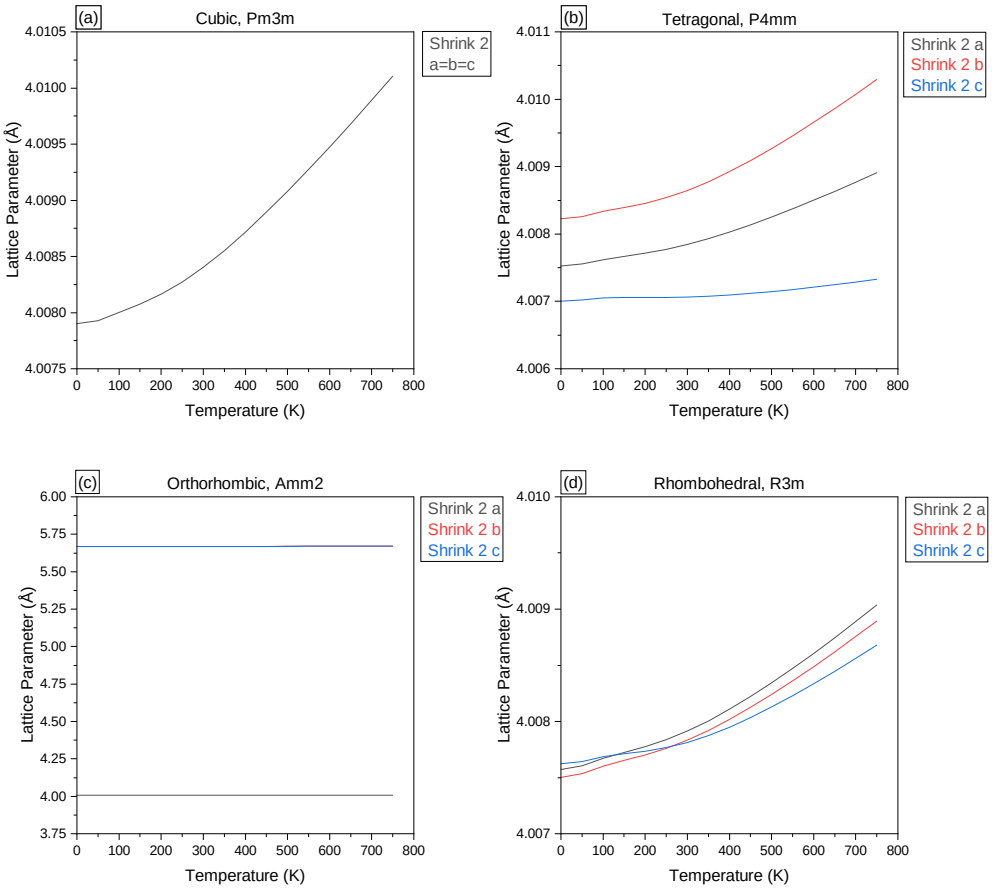

FIGURE 19 The fluctuation of the lattice parameter as a result of temperature, using the Freeman potentials for (a) cubic structure, Pm3m (b) tetragonal structure, P4mm (c) orthorhombic structure, Amm2 and (d) rhombohedral structure, R3m.

4.7 Further Analysis on the Tetragonal Structure

Of the three ferroelectric phases and the paraelectric phase, the only phase that isn't consistently accurate is the tetragonal phase, and since future research would be focused on the tetragonal to cubic structural phase transition, further scrutiny of the results for this structure is performed.

4.7.1 Volume and the c/a Ratio. Figure 20 shows the volume and c/a ratio of BTO at the ferroelectric to cubic phase transition. The tetragonal structure data in the operating temperature range is plotted, and then assumed

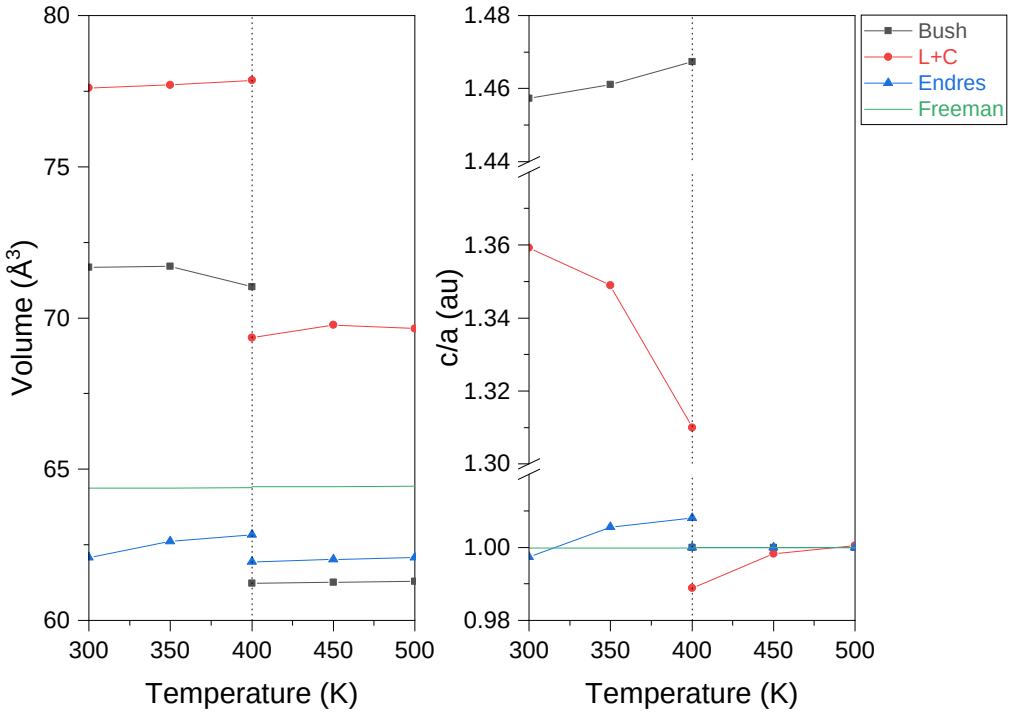

FIGURE 20 Volume of BTO (left) and the c/a axial range (right) as a function of temperature for the various potentials. The left half of each graph uses data from the tetragonal structures after optimisation, the right half takes the cubic data.

to change at the transition temperature to the cubic data. This is done to attempt to simulate what would happen experimentally.

Looking at the Bush and Lewis-Catlow potentials, it's clear they aren't suitable to be used for the tetragonal structure, as both the volume and the c/a ratio is too large. For the cubic structure the values for the volume aren't that close to the experimental value of 64.5Å[26], and for the c/a ratio, the Lewis-Catlow potentials have a value less than one which would not be true to a cubic structure, but the Bush potentials do. Overall, for these two structures, it isn't advised to use these sets of potentials, as they are not optimised to be used with them.

The Endres potential predicts smaller volumes than experimental and isn't suitable to describe the structure. However, in regard to the c/a value, there is promising results, as it does describe the values that are seen experimentally. But it must be remembered from figure 18 that the lattice parameters were changing by a good amount, and thus further repeat optimisation runs need to be performed in the hopes of achieving a more consistent and reliable optimisation. The Freeman potential accurately describes the volume seen in experiments but fails to replicate the c/a ration that describes the tetragonal structure. This potential is ideal for the cubic structure, but more revisions will need to be done for it to be satisfactory for the tetragonal structure.

4.7.2 The Role of the Potential Libraries. A lot of information is stored in the output file and provides information on how best to modify the input file to achieve the ideal results. It should be clear now that a big factor in the final structure is the interatomic potentials used rather than any keywords or options to be used with GULP.

Looking at the output files for the Freeman potentials, as soon as the first iteration of the optimisation algorithm has passed the tetragonal BTO structure has already immediately relaxed into a cubic structure. This is similarly shared by

the Endres potentials, though there are some strong fluctuations for some temperatures. The Lewis-Catlow and Bush potentials maintain a tetragonal structure but with a much larger c/a ratio than expected and shown experimentally. Ideally the final structure would maintain the crystal symmetry but with more appropriate values.

At this point, the most promising set of potentials to be used for the tetragonal structure is the Endres potentials. Although it may appear that while there are points in which the structure behaves tetragonally in figure 18[b], this is only due to the point at which the energy minimisation operation finished. By default, it's set to 1000, however, running these minimisations were proving very costly and so a maximum cycle was set to 20, where it is thought to be an appropriate compromise. This means that for most of the results, the true energy minimum wasn't found, and therefore the structure wasn't fully optimised. This is due to the soft phonons in the BTO structure, whereby the imaginary modes caused the number of modes to change. This can be described as a wall or barrier, presumably analogous to the transition state, in which the algorithm gets confused by the landscape on either side of the barrier and jump between the two sides, Ghosez et al. provide more information on this, as well as an accompanying graph[74, figure 3]. Consequently, the structure with its currents parameters would never truly optimise, just merely come close to the minimum. As a result, the point in which the minimisation was stopped determines the final structure. In the cases where the c/a values are larger for the tetragonal, this relates to the number of modes of the final structures, and as the number of modes fluctuate for each given run, whereby some may correlate to a tetragonal structure, or others to a cubic structure.

Table 4: The list of the species charges for the different interatomic potentials used throughout the project.

		Charge (|e|)			
Species	Core/Shell	Freeman	Endres	Lewis-Catlow	Bush
Ba	core	3.45	5.62	0.54	0.169
Ba	shell	-1.45	-3.76	1.46	1.831
Ti	core	4.0	4.76	1.11	2.327
Ti	shell	null	-1.58	2.89	1.673
O	core	0.472	0.91	0	0.513
O	shell	-2.472	-2.59	-2.00	-2.513

By comparing the interatomic potentials, shown in table 4 initially looking at the charges of the cores and shells of each ion, for the two files that behave relatively similarly for the tetragonal structure, the Freeman and the Endres interatomic potentials, they can be seen to share relatively similar potentials. Similar in the way in which they compare to other two, as most of the values are larger in magnitude for the Ba core and Ti core. This might be one of the causes for why these two potentials might default from a tetragonal structure to cubic one during the optimisation process. This can further be shown, as for the Lewis-Catlow and Bush potentials, which both behave similarly in which they are tetragonal but have a large c/a ratio, contrasting the behaviour of the other two potentials. However, upon changing the values in the Freeman library to the values that is utilized by Lewis-Catlow, there was still no tetragonal structure after optimisation for the range of temperatures. The only difference being that the c lattice parameter now more closely followed the trend of increasing in size seen by the a and c lattice parameters.

Another observation noticed about the libraries and their behaviour, is that for the Freeman and Endres potentials, where the tetragonal structure defaults to cubic, they both have negative charges for the Ba shell, and the Ti shell when used. The values for the charges in BTO are Ba2+, Ti^{4+} and $3O^{2-}$. For the Bush and Lewis-Catlow potentials, it achieves those cumulative charges for Ba and Ti by summing positively charged cores and shells to achieve the desired values. It could be that by assigning negatively charged values to the Ba and Ti shells, causes the structure to behave differently and collapse to a cubic structure. Implying the positively charged shells play an important role in the final structure having a tetragonal symmetry. It also must be noted that the Endres potentials do not explicitly have

the usual ionic charges for the constituent ions, but instead rather have $Ba^{1.86+}$, $Ti^{3.18+}$, and $3O^{1.68-}$ for a total overall charge of 0.

In the input file for the tetragonal structure, there is a difference specified between the oxygen ions, O1, and O2. The potential libraries do not distinguish between the 2 oxygen ions and essentially treats the same, applying the same parameters to each. As a result, the ions interact different than they do experimentally. It might be the case that specifying different values for the oxygen ions in the libraries would result in a tetragonal structure after optimisation.

Interestingly, in attempts to repeat the optimisation and thus average the results to achieve more reliable c/a value, showed that there isn't a randomness to the algorithm, and the same results would be shown depending on the number of cycles. With that in mind, it may be possible to add option words to change the minimisation technique at certain user defined points in the hopes of a more optimised structure. However, this proved challenging, first of all it would have been difficult to manually integrate for each chosen temperature and potential library, and so when a more generally defined process was used, in some cases the optimisation would fail. In some cases, the path at which the minimization travels along the energy landscape would essentially get trapped in the landscape, collapse and it would terminate, or for other cases, the number of modes drastically decreased by an order of magnitude until the optimisation failed.

Attempts to further improve optimisation were performed. The keywords "RFO" and "Transition_State", and "ZSISA" were applied to the input file for the tetragonal BTO phase for the Freeman and Endres potentials in the hopes that it would result in optimisation of tetragonal structures as opposed to cubic. During optimisation, the chosen phonon symmetry point was Γ, as when it was attempted to perform it over the path used previously, the optimisation failed to converge at all. When excluding that, the values did appear to converge, but were never truly optimised in the sense that it reached the maximum number of cycles (1000), or produced the error message:

```
Cycle:     292 Energy:     -160.113713  Gnorm:     0.000515  CPU:    95.396
** Hessian has required structure
Cycle:     293 Energy:     -160.113713  Gnorm:     0.000508  CPU:    95.692
** Hessian has required structure
**** Too many failed attempts to optimise ****
```

for example.

Nevertheless, it appears that given enough number of cycles to reach the Gnorm of 0, or increased the number of failed attempts to optimise, the structures should hopefully converge. However, in a positive light on this, the Freeman potentials finally produced a tetragonal structure, while the Endres failed to do so. The results are shown in table 5. The c/a result given from the Freeman potentials agree with experimental[26].

Ultimately, this result means that the Freeman potentials[69] are the best to be employed to reproduce each phase structure of BTO. The Endres[66] potentials fail for the tetragonal structure but perform admirably for the other

Table 5: The tetragonal structure optimised for a range of temperatures utilising the keywords zsisa, rfo, transition state.

	Freeman			Endres		
Temp	a	c	c/a	a	c	c/a
250	3.99248	4.01865	1.006554823	3.855071	3.307165	0.857873954
300	3.99252	4.01881	1.006584814	3.854732	3.30915	0.85846435
350	3.9926	4.01904	1.006622251	3.85437	3.311	0.859024951
400	3.99266	4.01925	1.006659721	3.853982	3.31275	0.859565509
450	3.99274	4.01949	1.00669966	3.853562	3.314406	0.860088926

structures. The older potentials utilizing work by Bush et al.[67], and Lewis and Catlow[62, 63, 68], do perform as well as the others, and in some cases just fail. Using all data gathered so far, shown in figure 21 is the variation of the a and c lattice parameters of BTO due to changing temperature, for each structural phase.

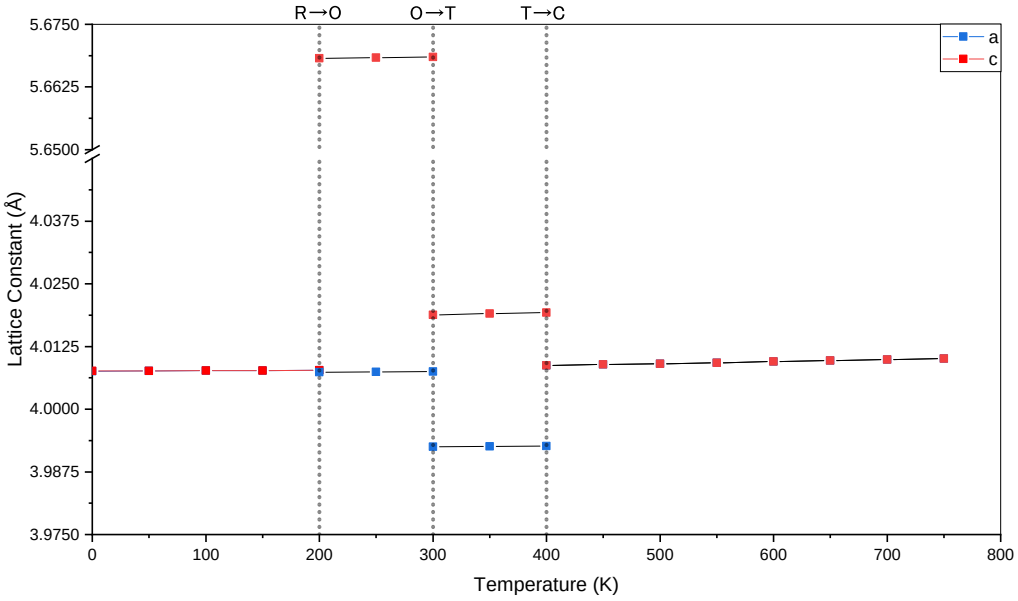

FIGURE 21 Diagram showing the variation of the lattice constants with temperature, using the interatomic potentials provided by Freeman et al.[69].

5 Conclusion

Multiple optimisation runs were carried out to further understanding of the roles the potentials play in optimisation different phase structures of BTO. Soft modes present in the structure which give rise to these phase transitions affect the ability of the algorithms used to optimise the structure. Four different potentials were used, three using only Buckingham potentials, with one using a combination of Buckingham, Lennard-Jones, and Three-body potentials.

It was that there was a division in the behaviour of the potentials, with the Bush and Lewis-Catlow potentials behaving similarly in comparison to the Endres and Freeman potentials that behaved differently for certain structures. Different aspects on the effects of the potentials were studying, using both internal and free energy, and it was found that the potentials each treat the structure differently due to the parameters defined in the library input.

The Bush potentials failed on most counts to reproduce expected structures for the phases, with lattice parameters having values much higher than expected for the cubic, tetragonal, and orthorhombic phases, in addition to warping the rhombohedral structure completely. The Lewis-Catlow fared better but could not replicate the tetragonal structure. Endres potentials provided better results for all structures, but compared to the Freeman potentials, was not as succinct and reliable. Ultimately, the Freeman potentials should be used for each phase of BTO, but due caution is needed in regard to how the input file for GULP is set up.

6 Future Work

Future work would be based upon using the potentials best chosen for each desired structure to expand the primitive lattice into a supercell and introduce twins into the structure. After completion of optimisation was satisfactory, other twin variations would be attempted, followed up by introducing defects that has been shown in literature to modify the Curie temperature. The causes of this would be investigated computationally to better understand the underlying cause. Further tests would be carried out on various twin domains of BTO in preparation for experimental work performed on BTO nanocrystals via coherent Bragg X-ray diffraction imaging.

References

(1) Von Hippel, A.; Breckenridge, R. G.; Chesley, F. G.; Tisza, L. *Ind. Eng. Chem.* **1946**, *38*, 1097–1109.

(2) Matthias, B.; von Hippel, A. *Phys. Rev.* **1948**, *73*, 1378–1384.

(3) Merz, W. J. *Phys. Rev.* **1949**, *76*, 1221–1225.

(4) Jaffe, H. *Ind. Eng. Chem.* **1950**, *42*, 264–268.

(5) Haertling, G. H. *J. Am. Ceram. Soc.* **1999**, *82*, 797–818.

(6) Waugh, M. D. *Electronic Engineering Times* **2010**, 34–36.

(7) Kishi, H.; Mizuno, Y.; Chazono, H. *Jpn. J. Appl. Phys.* **2003**, *42*, 1.

(8) Genchi, G. G.; Marino, A.; Rocca, A.; Mattoli, V.; Ciofani, G. *Nanotechnology* **2016**, *27*, 232001.

(9) Jaffe, B.; Cook William R., .; Jaffe, H. L., *Piezoelectric ceramics*; Academic Press London ; New York: 1971, ix, 317 p. :

(10) Acosta, M.; Novak, N.; Rojas, V.; Patel, S.; Vaish, R.; Koruza, J.; RossettiJr., G. A.; Rödel, J. *Applied Physics Reviews* **2017**, *4*, 041305.

(11) EU-Directive; 2002/95/EC *Off. J. Eur. Union* **2003**, *L37*, 24.

(12) EU-Directive; 2011/65/EU *Off. J. Eur. Union* **2003**, *L174*, 88.

(13) Saito, Y.; Takao, H.; Tani, T.; Nonoyama, T.; Takatori, K.; Homma, T.; Nagaya, T.; Nakamura, M. *Nature* **2004**, *432*, 84.

(14) Takenaka, T.; Maruyama, K.-i.; Sakata, K. *Jpn. J. Appl. Phys.* **1991**, *30*, 2236.

(15) Liu, W.; Ren, X. *Phys. Rev. Lett.* **2009**, *103*, 257602.

(16) Gao, J.; Xue, D.; Liu, W.; Zhou, C.; Ren, X. *Actuators* **2017**, *6*, DOI: 10.3390/act6030024.

(17) Harrington, S. A.; Zhai, J.; Denev, S.; Gopalan, V.; Wang, H.; Bi, Z.; Redfern, S. A. T.; Baek, S.-H.; Bark, C. W.; Eom, C.-B.; Jia, Q.; Vickers, M. E.; MacManus-Driscoll, J. L. *Nat. Nanotechnol.* **2011**, *6*, 491–495.

(18) Gale, J. D.; Rohl, A. L. *Molecular Simulation* **2003**, *29*, 291–341.

(19) Izyumskaya, N.; Alivov, Y.; MorkoÃ§, H. *Crit. Rev. Solid State Mater. Sci.* **2009**, *34*, 89–179.

(20) Han, W.; Zhu, J.; Zhang, S.; Zhang, H.; Wang, X.; Wang, Q.; Gao, C.; Jin, C. *J. Appl. Phys.* **2013**, *113*, 193513.

(21) Lines, M. E.; Glass, A. M., *Principles and Applications of Ferroelectrics and Related Materials*; Oxford University Press: Oxford, 2001, p 694.

(22) In *Ternary Compounds, Organic Semiconductors*, Madelung, O., Rössler, U., Schulz, M., Eds.; Springer Berlin Heidelberg: Berlin, Heidelberg, 2000, pp 1–6.

(23) Von Hippel, A. *Rev. Mod. Phys.* **1950**, *22*, 221–237.

(24) Devonshire, A. *London, Edinburgh Dublin Philos. Mag. J. Sci* **1949**, *40*, 1040–1063.

(25) Devonshire, A. *London, Edinburgh Dublin Philos. Mag. J. Sci* **1951**, *42*, 1065–1079.

(26) Nakatani, T.; Yoshiasa, A.; Nakatsuka, A.; Hiratoko, T.; Mashimo, T.; Okube, M.; Sasaki, S. *Acta Crystallographica Section B* **2016**, *72*, 151–159.

(27) Ravel, B.; Stern, E. A.; Vedrinskii, R. I.; Kraizman, V. *Ferroelectrics* **1998**, *206*, 407–430.

(28) Cochran, W. *Advances in Physics* **1960**, *9*, 387–423.

(29) Quittet, A.; Lambert, M. *Solid State Communications* **1973**, *12*, 1053–1055.

(30) Luspin, Y.; Servoin, J. L.; Gervais, F. *Journal of Physics C: Solid State Physics* **1980**, *13*, 3761.

(31) Comes, R.; Lambert, M.; Guinier, A. *Solid State Communications* **1968**, *6*, 715–719.

(32) Comès, R.; Lambert, M.; Guinier, A. *Acta Crystallographica Section A* **1970**, *26*, 244–254.

(33) Bersuker, I. *Physics Letters* **1966**, *20*, 589–590.

(34) Chaves, A. S.; Barreto, F. C. S.; Nogueira, R. A.; Ze ˜ks, B. *Phys. Rev. B* **1976**, *13*, 207–212.

(35) Yamada, Y.; Shirane, G.; Linz, A. *Phys. Rev.* **1969**, *177*, 848–857.

(36) Girshberg, Y.; Yacoby, Y. *Solid State Communications* **1997**, *103*, 425–430.

(37) Pirc, R.; Blinc, R. *Phys. Rev. B* **2004**, *70*, 134107.

(38) Merz, W. J. *Phys. Rev.* **1954**, *95*, 690–698.

(39) Pramanick, A.; Prewitt, A. D.; Forrester, J. S.; Jones, J. L. *Crit Rev Solid State* **2012**, *37*, 243–275.

(40) Likodimos, V.; Labardi, M.; Orlik, X. K.; Pardi, L.; Allegrini, M.; Emonin, S.; Marti, O. *Phys. Rev. B* **2001**, *63*, 064104.

(41) Mantri, S.; Oddershede, J.; Damjanovic, D.; Daniels, J. E. *Acta Mater.* **2017**, *128*, 400–405.

(42) Kay, H. F. *Acta Cryst.* **1948**, *1*, 229–237.

(43) Lee, T.; Aksay, I. A. *Cryst. Growth Des.* **2001**, *1*, 401–419.

(44) Qin, S.; Liu, D.; Zheng, F.; Zuo, Z.; Liu, H.; Xu, X. *Cryst. Eng. Comm.* **2010**, *12*, 3003–3007.

(45) Oppolzer, H.; Schmelz, H. *J. Am. Ceram. Soc.* **1983**, *66*, 444–446.

(46) Yu, Q.; Liu, D.; Wang, R.; Feng, Z.; Zuo, Z.; Qin, S.; Liu, H.; Xu, X. **2012**, *177*, 639–644.

(47) Cao, S.-G.; Wu, H.-H.; Ren, H.; Chen, L.-Q.; Wang, J.; Li, J.; Zhang, T.-Y. *Acta Mater.* **2015**, *97*, 404–412.

(48) Lee, B.-K.; Kang, S.-J. L. L. *Acta Mater.* **2001**, *49*, 1373–1381.

(49) Rečnik, A.; Bruley, J.; Mader, W.; Kolar, D.; Rahle, M. **1994**, *70*, 1021–1034.

(50) Ohsawa, T.; Hirose, S.; Ohashi, N. *Appl. Phys. Lett.* **2017**, *110*, 011604.

(51) Harris, D. T.; Burch, M. J.; Li, J.; Dickey, E. C.; Maria, J.-P. *J. Am. Ceram. Soc.* **2015**, *98*, 2381–2387.

(52) Cheng, S.-Y.; Ho, N.-J.; Lu, H.-Y. *J. Am. Ceram. Soc.* **2006**, *89*, 2177–2187.

(53) An, S.-M.; Kang, S.-J. L. *Acta Mater.* **2011**, *59*, 1964–1973.

(54) Nelson, S. A. Twinning, Polymorphism, Polytypism, Pseudomorphism: Twinning in Crystals., 2013.

(55) Lee, B.-K.; Chung, S.-Y.; Kang, S.-J. L. *Acta Mater.* **2000**, *48*, 1575–1580.

(56) Cao, W.; Cross, L. *Physical Review B* **1991**, *44*, 5.

(57) Megaw, H., *Ferroelectricity in crystals*; Methuen: London, 1957.

(58) Dudhe, C. M.; Nagdeote, S. B.; Khambadkar, S. J.; Arjunwadkar, P. R.; Patil, R. R. *Ferroelectrics* **2014**, *471*, 148–155.

(59) Randall, C.; Barber, D.; Whatmore, R. *J. Mater. sci.* **1987**, *22*, 925–931.

(60) Jang, J.; Cho, W.; Lee, J.; Choi, S.; Hahn, T. *Jpn. J. Appl. Phys.* **1997**, *36*, 6942.

(61) Kraševec, V.; Drofenik, M.; Kolar, D. *J. Am. Ceram. Soc.* **1990**, *73*, 856–860.

(62) Lewis, G.; Catlow, C. *Journal of Physics and Chemistry of Solids* **1986**, *47*, 89–97.

(63) Lewis, G. V.; Catlow, C. R. A. *Journal of Physics C: Solid State Physics* **1985**, *18*, 1149.

(64) Deacon-Smith, D. STRUCTURE PREDICTION OF PEROVSKITE SURFACES AND NANOCLUSTERS., `http://discovery.ucl.ac.uk/id/eprint/1472780` (accessed 09/21/2018).

(65) Sepliarsky, M.; Asthagiri, A.; Phillpot, S.; Stachiotti, M.; Migoni, R. *Current Opinion in Solid State and Materials Science* **2005**, *9*, 107–113.

(66) Endres, F.; Steinmann, P. *GAMM-Mitteilungen*, *38*, 132–146.

(67) Bush, T. S.; Gale, J. D.; Catlow, C. R. A.; Battle, P. D. *J. Mater. Chem.* **1994**, *4*, 831–837.

(68) *Proceedings of the Royal Society of London A: Mathematical, Physical and Engineering Sciences* **1977**, *353*, 533–561.

(69) Freeman, C. L.; Dawson, J. A.; Chen, H.-R.; Harding, J. H.; Ben, L.-B.; Sinclair, D. C. *J. Mater. Chem.* **2011**, *21*, 4861–4868.

(70) Wyckoff, R., *Crystal Structures*; Crystal Structures v. 2; Interscience Publishers: 1960.

(71) Persson, K. Materials Data on BaTiO3 (SG:99) by Materials Project., An optional note, 2014.

(72) Kwei, G. H.; Lawson, A. C.; Billinge, S. J. L.; Cheong, S. W. *The Journal of Physical Chemistry* **1993**, *97*, 2368–2377.

(73) Shanno, D. F. *Mathematics of Computation* **1970**, *24*, 647–656.

(74) Ghosez, P. H.; Gonze, X.; Michenaud, J. P. *Ferroelectrics* **1998**, *206*, 205–217.

A GULP Library Files

A.1 Bush Library File

Library file utilizing a paper by Bush et al. [67]:

```
species
Ba core   0.169
Ba shel   1.831
Ti core   2.327
Ti shel   1.673
O  core   0.513
O  shel  -2.513
buckingham
Ba shel O shel   4818.416 0.3067   0.00 0.0 10.0
Ti shel O shel   2088.107 0.2888   0.00 0.0 10.0
O  shel O shel     25.410 0.6937  32.32 0.0 12.0
spring
Ba   34.05
Ti  253.60
O    20.53
```

A.2 Lewis and Catlow Library

Library file utilizing a combination of papers by Lewis and Catlow [62, 63, 68]:

```
#
#  from G.V.Lewis and C.R.A.Catlow 1985
#  Lewis and Catlow 1985
#  Catlow 1977
#
species
Ba    core    0.540
Ba    shel    1.460
Ti    core    1.110
Ti    shel    2.890
O     core    0.000
O     shel   -2.000
buckingham
Ba     shel  O    shel     931.7    0.3949     0.0      0.0  12.0
#Cutoff 6  ---> 12
Ti     shel  O    shel     754.2    0.3879     0.0      0.0  12.0
O      shel  O    shel   22764.3    0.1490    43.0      0.0  12.0
# C=20.4 for O-O according to Catlow 1977

spring
Ba     14.74
#O      70.39
O      80.21
#O      86.40
Ti     37.30
#O     210.02
```

A.3 Endres Library

Library file using potentials from Endres and Steinmann [66]:

```
#
# Library file for Barium Titanate, BaTiO3
# Florian Endres, Paul Steinmann, Molecular statics simulations of
# ferroelectric barium titanate in the rhombohedral phase.
#
species
Ba core   5.62
Ba shel  -3.76
Ti core   4.76
Ti shel  -1.58
O  core   0.91
O  shel  -2.59
buck
Ba  shel O  shel   864.536   0.38729   0.0     0.0 12.0
Ti  shel O  shel  4526.635   0.25239   0.0     0.0 12.0
O   shel O  shel  4102.743   0.29581 300.0     0.0 12.0
spring
O    31.0
Ba  251.8
Ti  321.0
```

A.4 Freeman Library

Library file utilizing a recent paper by Freeman et al. [69]:

```
#
# Library file for Barium Titanate, BaTiO3
# A new potential model for barium titanate and its implications for
# rare-earth doping
# Colin L. Freeman,* James A. Dawson, Hung-Ru Chen, John H. Harding,
# Liu-Bin Ben and Derek C. Sinclair
#
species
Ba core    3.45
Ba shel   -1.45
Ti core    4.0
O  core    0.472
O  shel   -2.472
buck
Ba shel O shel  1150.0   0.38037  55.0  0.0 12.0
O  shel O shel 22764.0   0.14900  43.0  0.0 12.0
Lenn 7 6
Ti core O shel  1234.07379  471.92114  0.0 12.0
#Lenn epsilon 7 6
#Ti core O shel  0.01153  5.230   0.00 12.00
three
Ti core O core O core 1.82  90.0  2.5 2.5 3.5
spring
Ba 56.23
O  15.41
```

A.5 Cubic Structure

```
cell
4.0118 4.0118 4.0118
```

```
fractional
Ba core  0.0     0.0     0.0
Ti core  0.5     0.5     0.5
O  core  0.0     0.5     0.5
O  core  0.5     0.0     0.5
O  core  0.5     0.5     0.0
Ba shel  0.0     0.0     0.0
Ti shel  0.5     0.5     0.5 #remove for Freeman Library
O  shel  0.0     0.5     0.5
O  shel  0.5     0.0     0.5
O  shel  0.5     0.5     0.0
```

A.6 Tetragonal Structure

```
4.002  4.002  4.216  90.0  90.0  90.0
fractional
Ba core  0.0     0.0     0.0202
Ti core  0.5     0.5     0.5389
O1 core  0.5     0.5     0.9708
O2 core  0.5     0.0     0.4920
O2 core  0.0     0.5     0.4920
Ba shel  0.0     0.0     0.0202
Ti shel  0.5     0.5     0.5389 #remove for Freeman Library
O1 shel  0.5     0.5     0.9708
O2 shel  0.5     0.0     0.4920
O2 shel  0.0     0.5     0.4920
```

A.7 Orthorhombic Structure

```
cell
3.990  5.669  5.682   90.0  90.0  90.0
fractional
Ba core  0.0     0.0     0.0
Ba core  0.0     0.5     0.5
Ti core  0.5     0.0     0.510
Ti core  0.5     0.5     1.010
O1 core  0.0     0.0     0.490
O1 core  0.0     0.5     0.990
O2 core  0.5     0.253   0.237
O2 core  0.5    -0.253   0.237
O2 core  0.5     0.753   0.737
O2 core  0.5     0.247   0.737
Ba shel  0.0     0.0     0.0
Ba shel  0.0     0.5     0.5
Ti shel  0.5     0.0     0.510  #remove for Freeman Library
Ti shel  0.5     0.5     1.010  #remove for Freeman Library
O1 shel  0.0     0.0     0.490
O1 shel  0.0     0.5     0.990
O2 shel  0.5     0.253   0.237
O2 shel  0.5    -0.253   0.237
O2 shel  0.5     0.753   0.737
O2 shel  0.5     0.247   0.737
```

A.8 Rhombohedral Structure

```
cell
```

```
4.00360 4.00360 4.00360 89.839 89.839 89.839
fractional
Ba core  0.0000  0.0000  0.0000
Ti core  0.4872  0.4872  0.4872
O  core  0.0193  0.5109  0.5109
O  core  0.5109  0.0193  0.5109
O  core  0.5109  0.5109  0.0193
Ba shel  0.0000  0.0000  0.0000
Ti shel  0.4872  0.4872  0.4872  #remove for Freeman Library
O  shel  0.0193  0.5109  0.5109
O  shel  0.5109  0.0193  0.5109
O  shel  0.5109  0.5109  0.0193
```

B Typical Keyword Input File

```
opti conp comp prop static_first free phonon eigenv dist
#rfo transition_state zsisa
#single conp comp prop dist phonon eigenv
cutd 4
cell
4.002 4.002 4.216 90.0 90.0 90.0
fractional
Ba core  0.0     0.0     0.0202
Ti core  0.5     0.5     0.5389
O1 core  0.5     0.5     0.9708
O2 core  0.5     0.0     0.4920
O2 core  0.0     0.5     0.4920
Ba shel  0.0     0.0     0.0202
Ti shel  0.5     0.5     0.5389
O1 shel  0.5     0.5     0.9708
O2 shel  0.5     0.0     0.4920
O2 shel  0.0     0.5     0.4920
lib Library.lib
temp 150
shrink 2
# G X M G R X
kpoints 6
0.0 0.0 0.0
0.0 0.5 0.0
0.5 0.5 0.0
0.0 0.0 0.0
0.5 0.5 0.5
0.0 0.5 0.0
dispersion 1 60
0.0 0.0 0.0 &
to 0.0 0.5 0.0 &
to 0.5 0.5 0.0 &
to 0.0 0.0 0.0 &
to 0.5 0.5 0.5 &
to 0.0 0.5 0.0
output phon phon
accuracy 20.000  4 20
xtol 20
ftol 20
gtol 12
#switch_min rfo  gnorm     0.05
```

```
#switch_min rfo cycle 50
#maximise mode 382
#lowest_mode 0 362
maxcyc 20
dump output.gin
```

C Bush Interaction With Dispersion Curve

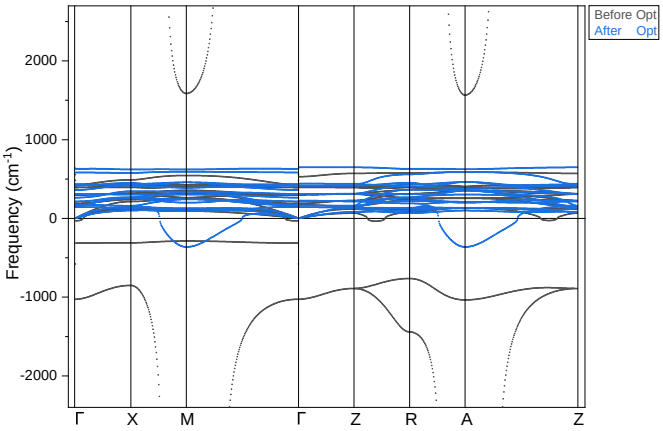

FIGURE 22 Phonon dispersion curve for the tetragonal structure using Bush's potential, highling one of the modes undergoing an extreme fluctuation for a single run without optimisation.

D Experimenting with Transition State Keyword

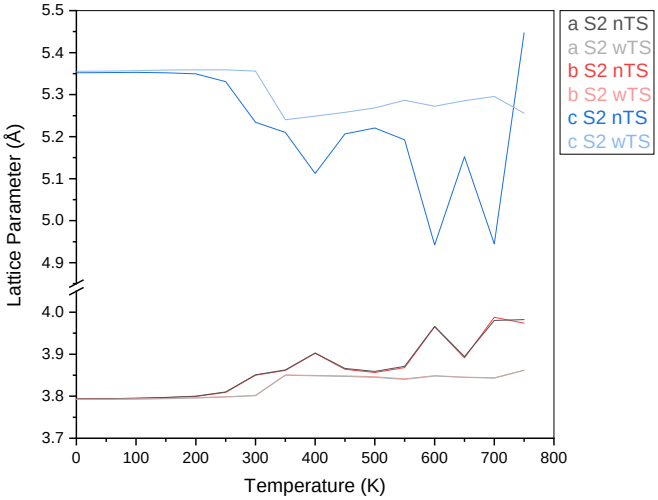

FIGURE 23 For tetragonal BaTiO3 using Lewis and Catlow potentials